Electro-reduction of NO_x-species in alkaline medium at modified carbon-supported palladium nanoparticles with variable concentration of C-sp^2: An in-situ mass-spectrometry approach

S. Vázquez-Bautista [a], E. Ramírez-Meneses [a,*], A. Manzo-Robledo [b,*], G. Zacahua-Tlacuatl [c], L. Lartundo-Rojas [d], J. Acosta-Jara [e], L.L. Pedraza-Segura [a], M. Luna-Trujillo [b]

[a] *Universidad Iberoamericana, Departamento de Ingeniería Química, Industrial y de Alimentos, Prolongación Paseo de la Reforma 880, Lomas De Santa Fe, 01219 Ciudad de México, Mexico*
[b] *Instituto Politécnico Nacional, Escuela Superior de Ingeniería Química e Industrias Extractivas (ESIQIE-IPN). Departamento de Ingeniería Química SEPI, Unidad Profesional Adolfo López Mateos, 07738 Ciudad de México, Mexico*
[c] *Instituto Politécnico Nacional, Laboratorio de Posgrado de Operaciones Unitarias-ESIQIE, UPALM, Zacatenco, Col. Lindavista, Ciudad de México, CP 07738 Ciudad de México, Mexico*
[d] *Instituto Politécnico Nacional, Centro de Nanociencias y Micro y Nanotecnologías, UPALM Zacatenco, CP 07738 Ciudad de México, Mexico*
[e] *Universidad ESAN, Alonso de Molina, 1652, Monterrico, Surco, Lima, Perú*

ARTICLE INFO

ABSTRACT

Electrochemical denitrification is a promising technology for removing NO_x species due to its environmental impact. In this work, nanostructured palladium electrocatalysts (3.2–3.7 nm) stabilized with different compounds namely lignin, oleylamine, octylamine, and 2-methyl-2butanol supported on Vulcan carbon were synthesized from organometallic precursors for the electrocatalytic reduction of nitrated species. For this purpose, electrochemical techniques such as cyclic voltammetry at different concentrations of $NaNO_2$ and $NaNO_3$ (saturated with NO_2 gas, synthesized in situ) in the alkaline medium were carried out. The current versus potential characteristic (i-E) showed that the as-synthesized Pd/lignin/C catalyst exhibited the highest activity in the reduction of NO_2^- and NO_3^-, with hydrogen production at more negative potentials, as demonstrated by differential electrochemical mass spectroscopy (DEMS). Additionally, scanning electron microscopy (SEM), transmission electron microscopy (TEM), X-ray diffraction (XRD) and X-ray photoelectron spectroscopy (XPS) indicate the presence of metallic palladium and other Pd_yO_x species well distributed on the carbon support matrix promoting different interfacial redox processes depending on the stabilizer in turn and the carbon hybridization namely, D-parameter ($D = sp^2/sp^3$).

1. Introduction

In recent years, the elimination of pollutants in the air, particularly those related to NO_x, continues to be one of the major environmental challenges. To solve this problem, the use of electrochemical techniques for NO_x reduction is an excellent alternative. For example, reducing climate change (accelerated by anthropogenic activities) is one of the most urgent challenges facing humanity. Dependence on fossil fuels for energy production causes the concentration of greenhouse gases (GHGs) to increase mainly in areas with high population density. The chemical composition of air pollution contain, for example, ozone and volatile organic compounds such as SO_x, NO_x, CO_x [1]. Population growth,

urbanization and the environmental impact suffered by ecosystems connected to urban areas are considerably demanded [2]. These variables directly affect hydrological mechanisms as urban stormwater runoff is an important source of water pollution. Urbanization also leads to water contamination by suspended sediments, heavy metals, hydrocarbons, nutrients, and pathogens [3]. The composition of affected water resources, mainly of species related to human health, has been monitored [4]. High concentrations of nitrogenous species affect human health. However, similar effects have been reported during long exposure with lower concentrations of these species [5]. Nitrogenous species (i.e. NO_2^-) that are ingested and reach the intestinal tract cause methemoglobinemia [6]. In this context, the microorganisms presented in the

---

gastrointestinal system reduce the ingested nitrate ions (NO_3^-) to NO_2^-, (which is incorporated into hemoglobin), oxidizing ferrous ions in ferric ions, and then forming methemoglobin. If the methemoglobin concentration is high, an oxygen-transfer interruption between blood cells is observed, causing methemoglobinemia disease[6]. The global health organization has established a recommended maximum (MCL) of 50 mg/L for NO_3^- and 30 mg/L for NO_2^- in drinking water [7]. Whereas, the U.S. Protection Agency established a lower MCL of 10 mg/L for NO_3^- and 1 mg/L for NO_2^- [8]. Physicochemical methods such as ion exchange, reverse osmosis [9], catalysis [10], and electrodialysis [11]; and biological methods including denitrification [12], autotrophic denitrification [13], and heterotrophic [14] have been proposed. On the other hand, electrochemical methods offer procedures that do not require prior conditioning of contaminated effluents or remove large volumes of sludge, brine or solid residues from the products obtained [15]. The electrochemical reduction reaction of nitride species has been extensively investigated because they can be reduced to different products. Electrochemical reduction of these species is a process involving mass transfer and multi-electronic transfer process, where a variety of very stable intermediate species can be produced, depending on the catalyst employed. One of the factors that can improve the performance of an electrocatalytic material is the synthesis method, as it is possible to control structural and morphological properties as well as the modulation-interaction of the obtained nano-material with the support-surface matrix [16].

Then during synthesis, precursors, and support (or supports) interact to give unique characteristics to the final product. Therefore, for such an approach, the control of the reaction conditions during synthesis could affect the selectivity and conversion (from particles size, morphology, and structural characteristic) for the electrochemical reduction of, for example, NO_x-species [17]. In order to develop more active, selective and stable electro-catalysts a wide variety of monometallic, bimetallic, and tri-metallic materials have been synthesized: Cu-Zn/γAl$_2$O$_3$ [18], Fe-Mo/ZSM-5 [19], Pd/YSZ [20], Mn-Ce/TiO$_2$, Pt/Al$_2$O$_3$ [21], Cu/ZrO$_2$/Al$_2$O$_3$ [22], Ag-Al$_2$O$_3$ [23], Pd/Vulcan [24], Pd-Ag/carbon xerogels [25], Pd/C and Pd/Vulcan [26], Pt/C [27], Pt/Vulcan-ETEK [28], Pt/Vulcan [29], Pt/Vulcan and Pt-Rh/Vulcan [30], Pt/C-ETEK [31], Pd/C and Pd-Cu/C [32], among others. Also, a variety of supports-materials (e.g., carbon structures) have been used to obtain a good metallic-nanoparticles dispersion and to improve charge transfer process. In addition, palladium-based nanomaterials as an active phase have been shown to be versatile and selective catalysts towards nitrogen generation during the electrochemical reduction of NO_3^-, and NO_2^- [33]. As metallic palladium (and other Pd-oxide species) at nanometric scale are attached to the XC-72R Vulcan-carbon support, the electronic properties of the formed composite are favored by the surface area (ca. 250 m^{2}g^{-1}), good electrical conductivity (ca. 4 S cm^{-1}), alteration of the hybridization ratio (sp^3/sp^2) [34], a relative good corrosion resistance, and good stability [35]. On the other hand, it is well known that stabilizer could modify some morphological-structural and electronic properties of the formed composite. Stefano Diodati, et al., reported that the correlation of the results between the chemical analysis, mainly X-ray photoelectron spectroscopy (XPS), and the electrochemical results allowed the understanding of the interaction between the synthesis parameters, and the chemical composition of the electrocatalyst surface, identifying the effects of the metallic-species formed during the synthesis. Surface composition and chemical nature of the species presented in the synthesized materials allow to major understand the role of the support-matrix in the reaction [36] linked with electronic effects (affecting active-sites distribution) and selectivity-conversion towards specific product [37]. Moreover, palladium and palladium-based nanoparticles have been widely reported as electrocatalytic materials demonstrating very good selectivity and high conversion [38] for reactions with organic compounds such as alcohol oxidation, glucose oxidation [39], formic acid oxidation [40], urea oxidation [41], oxygen

reduction [42], CO$_2$ reduction [24], NO$_x$ reduction [26], and for fuel cell applications [43], [44].

In this work, nanostructured palladium electrocatalysts stabilized with different compounds (lignin, oleylamine, octylamine, and 2-methyl-2-butanol) and supported on Vulcan carbon were evaluated in the electrochemical reduction of nitrates species. From the current versus potential (i-E) characteristics obtained using cyclic voltammetry, it has been demonstrated that, among all the stabilizers employed, lignin prepared-palladium electrocatalyst exhibited the better activity towards the electrochemical reduction reaction of NO_3^- and NO_2^-, as also verified using on-line differential electrochemical mass spectroscopy (DEMS) for selected species.

On the other hand, XPS and X-ray diffraction (XRD) revealed that the variation of the sp^3/sp^2 carbon ratio, the presence of zero-valent palladium and well-distributed Pd$_y$O$_x$ species on the Vulcan carbon support, promote different redox-interfacial processes associated with the nature of the stabilizer employed.

2. Experimental section

Bis (dibenzylideneacetone) palladium (0), (Pd(dba)$_2$, 99 %, Sigma-Aldrich); nitrogen (N$_2$, 99 %, INFRA); dihydrogen (H$_2$, 99.97 %, INFRA); oleylamine (CH$_3$(CH$_2$)$_7$CH-CH(CH$_2$)$_7$CH$_2$NH$_2$, 99 %, Aldrich); octylamine (CH$_3$(CH$_2$)$_7$NH$_2$, 99 %, Aldrich); 2-methyl-2-butanol (C$_5$H$_{12}$O, 99 % Sigma-Aldrich) and anhydrous n-pentane (C$_5$H$_{12}$, 99 %, Sigma-Aldrich) were employed without further purification.

The stabilizer lignin was extracted from corn-cob using two consecutive pretreatments. First, corn-cob was ground to ca. 2.38 mm (US mesh #8) with hammer mill grinder. Then, the material was pre-treated from thermochemical process [45] resulting in the hydrolysis of the hemicellulose (75–80 %) and acid soluble lignin (~85–95 %). This process generates two effluents: a pentose-rich sirup and a solid material named corn-cob, which is processed in an alkaline/peroxide media (10–16% w/v) for 1 h at 55 °C and in at a stirring speed environment at 160 rpm. From this last process, two streams were obtained a solid material rich in cellulose (80–90 %) and a liquid effluent containing solubilized lignin-xylan mixture. Alkaline lignin was recovered by precipitation from the liquid stream, adding a solution of acetic acid 50 %. Thereafter, it was separated from the acid liquor (pH 4–3), dried at 105 °C for 12 h and milled until reach a size of ca. 1 mm. Solid lignin was washed twice with a sulfuric acid solution (pH 4, 1:10 w/v). Purified lignin was recovered by centrifugation and dried at 105 °C for 12 h. Purified alkaline lignin is a set of phenolic compounds of different molecular weight and structure; to obtain a lignin fraction useful as a stabilizer for synthesis of nanoparticles, the material would be soluble in alcohols, aliphatic or cyclic ethers. Therefore, a suspension of alkaline lignin with absolute methanol (1:10 w/v) was stirred for 12 h. The suspension was separated by centrifugation; the supernatant was concentrated using a rotatory evaporator and dried at 80 °C for 12 h. The obtained lignin was identified using Fourier transform infrared spectroscopy and proton nuclear magnetic resonance spectroscopy [46].

2.1. Synthesis of Pd/stabilizer/C

Palladium nanoparticles were synthesized using the method of ligands displacement of organometallic precursors following the standard technique with a Fisher-Porter reactor and Schlenk tubes under nitrogen atmosphere; Pd(dba)$_2$ was used as precursor. Lignin functionalized with methanol obtained from corn-cob, oleylamine, octylamine, and 2-methyl-2-butanol were used as stabilizers. Vulcan carbon was used as support, and dihydrogen was used as reaction gas.

In order to prepare Pd/oleylamine/C, Pd/octylamine/C or Pd/2-methyl-2-butanol, 0.7826 mmol of Pd(dba)$_2$ and 0.7496 g of Vulcan carbon, were introduced to the reactor at constant stirring using a magnetic bar. Thereafter, and maintaining a nitrogen atmosphere, 0.5167 mL of oleylamine, 0.2594 mL of octylamine or 0.1701 mL of 2-

methyl-2-butanol were added as stabilizer in turn. The molar ratio metal:stabilizer was 1:2 in 60 mL of THF except for lignin where the weight percent ratio metal:lignin was 1:10 having 0.0555 mol Pd(dba)$_2$ and 0.5 g of Vulcan carbon. Then, at room temperature, the reagent mixture was pressurized with dihydrogen at 3 bars for 20 h under stirring in the Fisher-Porter reactor. Fig. 1 present the general reaction scheme for all synthesis. Among other, the stabilizers play an important role in the modulation of the metallic-particles size-distribution, also avoiding their agglomeration. After the reaction time, the reactor was depressurized, and the colloidal solution was concentrated under vacuum. In addition, by products were removed with a series of three 20 mL washes with anhydrous n-pentane. Finally, the precipitate was dried under vacuum. In all cases, the catalysts were obtained having a metal: support ratio of 10:90 (wt%).

2.2. Structural and morphological characterization of Pd/stabilizer/C

The crystal structure of the Pd/stabilizer/C materials was determined using a Bruker D8 Advance diffractometer with Cu Kα radiation ($\lambda_{Cu} = 1.54$Å) with a Ni filter operating in the theta-theta setting at 35 kV. The diffractograms were obtained in the 2θ range of 20–90° with a scanning speed of 0.4° min-1 with an angular resolution of 0.02° step. TEM images showing the morphology and distribution of stabilized-palladium nanoparticles on the carbon support were examined using the TEM technique with a Titan microscope operating at 300 kV. The samples were prepared by evaporation at room temperature, with one drop of colloidal suspension of each Pd/stabilizer/C material in ethanol, deposited on a carbon coated copper grid. Textural characteristics (specific surface area, pore size, and pore volume) of catalysts were determined using nitrogen adsorption measurements at low pressure and 77 K. The analysis was carried out using an Autosorb iQ from Quantachrome equipment. The electronic properties and oxidation states of the as-synthesized stabilized Pd nanoparticles supported on Vulcan carbon were investigated from XPS analysis. The analysis was performed using a K-alpha Thermo Fischer Scientific spectrometer with a monochromatic Al Kα source (1486.6 eV). General and high-resolution spectra were generated using an X-ray spot size of 400 μm at 160 and 45 eV pass- energy, respectively. The samples remained under vacuum for more than 10 h in a pre-chamber directly connected to the equipment, then transferred to the analysis chamber-zone with a base pressure of 1×10^{-9} Torr that remains constant throughout the experiment. Core-level spectra were deconvoluted with Thermo Fisher Scientific's AVANTAGE V5.97 software using a Shirley-type background subtraction and a pseudo-Voigt function with Gaussian (30 %)-Lorentzian (70 %) for each component.
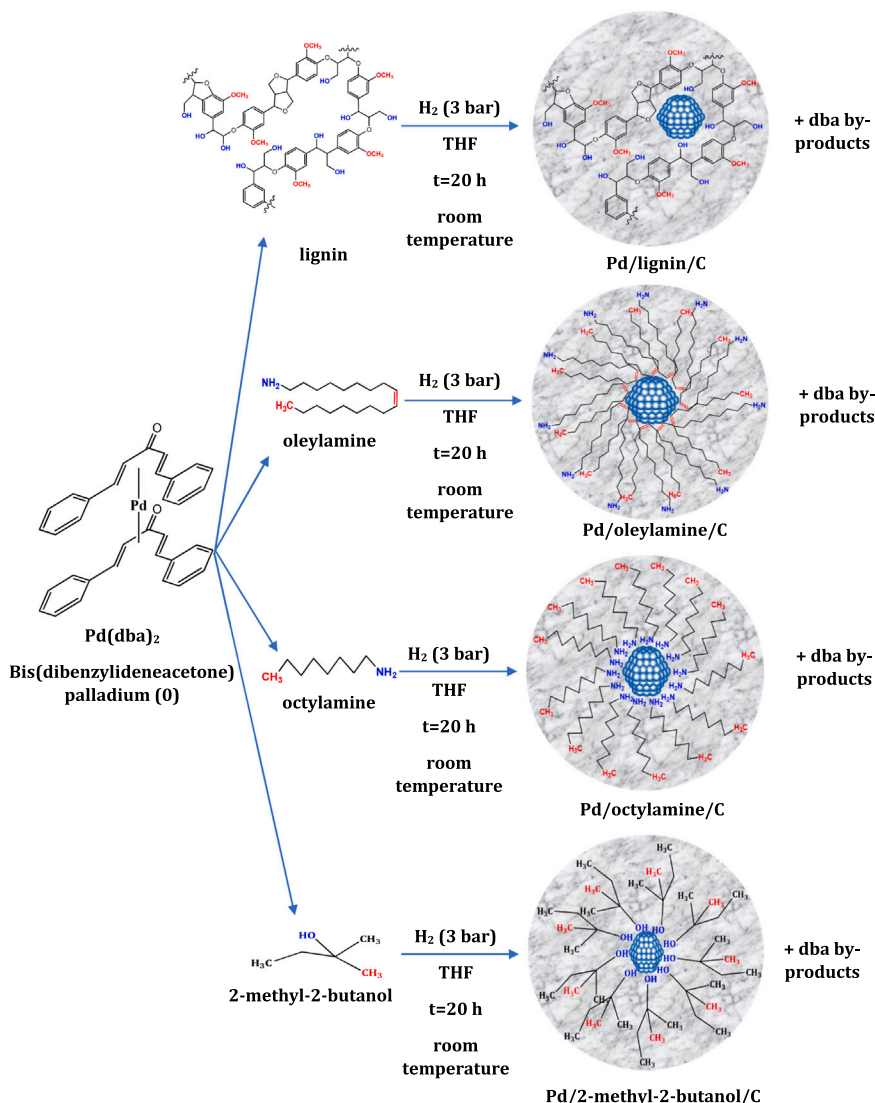

Fig. 1. General scheme showing the synthesis-reaction pathway and proposed stabilization of metal nanoparticles.

2.3. Electrochemical measurements

Electrochemical evaluation was performed using an EG&G potentiostat/galvanostat (Princenton Applied Research, model 263A) and a three-electrode electrochemical cell. A glassy carbon bar (GC, 0.0707 cm^2) served as a working electrode. The cross-section area of the GC was polished with an alumina (ca. 0.3 μm) suspension and rinsed with deionized water (DI water, 18.2 MΩ). A reversible hydrogen electrode (RHE, 0.5 M H$_2$SO$_4$) and a graphite bar were used a reference electrode and counter-electrode, respectively. The catalyst suspensions of Pd/stabilizer/C (weight percent ratio 90:10 Vulcan carbon:metal) were prepared by ultrasonically mixing 70% v/v DI water, 24 % v/v isopropanol (99.5 %, Meyer) and 6 % v/v Nafion (Aldrich) for 120 min. Then, 5 μL of each suspension was, in turn, deposited on the cross section of the glassy carbon electrode. Prior to each electrochemical evaluation, the working electrode was subject to cyclic voltammetry (CV) polarization-scan in an argon-gas saturated 0.5 M NaOH solution.

After thirty cycles at a scan rate of 100 mVs^{-1} in a potential window from 0.7 to − 0.85 V/RHE, and starting at open circuit potential, stable current versus potential redox-profiles (i-E) were obtained depending on the Pd/stabilizer/C sample in turn. The electrochemical active surface area (ECSA) of the PdO$_{red}$ absorbed monolayer for each Pd/stabilizer/C material was calculated using CV measurement in a NaOH 0.5 M solution at a scan rate of 100 mVs^{-1} varying the shifting potential from the anodic-scan zone. On the other hand, the DEMS technique for in-situ detection of species generated during the faradic process was employed. For such an approach the electrochemical cell was connected to a quadrupolar mass spectrometer (Prisma Plus QMG220). The interface between the cell and the vacuum system consists of a teflon-porous membrane (75 % porosity, 60 μm thick and 0.2 mm pore diameter). The working electrode was prepared as describe above. The ion current from mass to charge ratios (m/z) for selected species were recorded simultaneously with the faradic-current characteristic at scan rate of 2 mVs^{-1} in a saturated electrolyte with NO$_{2(g)}$ for 10 min, the potential window was fixed from 0.7 to − 0.85 V/RHE in a NaOH 0.5 M + NaNO$_2$ 0.5 M (or NaNO$_3$ 0.5 M) solutions. The working pressure in the detector chamber was ca. 10^{-5} mbar for all experiments.

For the in-situ synthesis of NO$_{2(g)}$ 0.8 mg of metallic Cu (Condumex, 99.9%) was diluted in 6.4 mL of HNO$_3$ (Sigma-Aldrich, 70 %). The NO$_{2(g)}$ produced was injected for 10 min at the working solution in turn: NaNO$_3$ and/or NaNO$_2$ in NaOH 0.5 M as supporting electrolyte. During the dilution of metallic copper in nitric acid an exothermic reaction is carried out. During this reaction, the solution changes to an intense brown-like color, indicating the production of NO$_{2(g)}$. according to Eq. (1) [47], [48].

$$Cu + 4HNO_3 \rightarrow Cu(NO_3)_2 + 2H_2O + 2NO_2 \qquad (1)$$
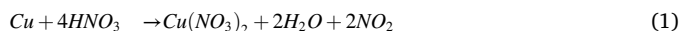
3. Results and discussions

3.1. X-ray diffraction

Fig. 2 shows the X-ray diffraction patterns of Pd/lignin/C, Pd/oleylamine/C, Pd/octylamine/C, Pd/2-methyl-2-butanol/C and Vulcan carbon (for reference). The diffraction peaks of the powders at 2θ = 40.11°, 46.66°, 68.08° and 82.09° correspond to the (111), (200), (220) and (311) planes, respectively; resulting in a palladium face-centered cubic structure (JCPDS 46–1043) [49]. The diffraction peaks between 20° and 45° (2θ) are assigned to Vulcan carbon support.

The average crystallite size was obtained with Scherrer (Eq. (2)) using the main-palladium peak corresponding to the (111) plane in Fig. 2.

$$d = \frac{K \bullet \lambda}{B \bullet cos\theta} \qquad (2)$$

Where d is the crystallite size, K is the shape factor having values from
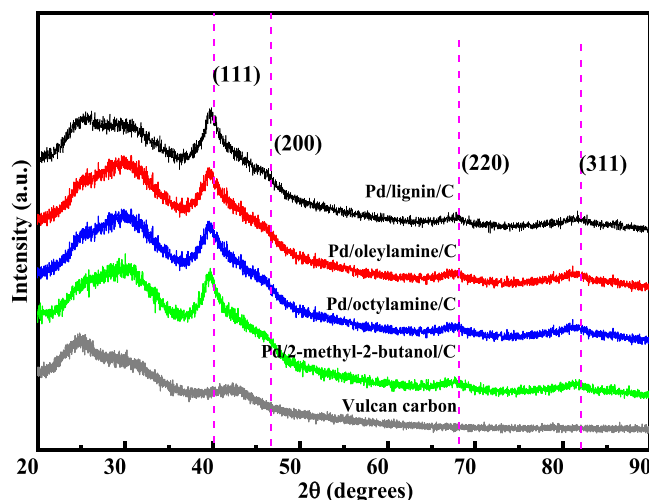

Fig. 2. X-ray diffraction patterns of Pd/lignin/C, Pd/oleylamine/C, Pd/octylamine/C, Pd/2-methyl-2-butanol/C and carbon Vulcan XC-72R.

0.89 to 1.39, λ is the wavelength of X-rays radiation, θ is the diffraction angle position, and B is full width at half maximum (FWHM) of the diffraction peak at the 2θ angle (radians) [50]. The results of phase identification, crystallite size and changes in lattice parameters were determined by X-ray diffraction and Rietveld refinements. The synthesis method used produces particles in the nanometric scale from 3.6 to 5.4 nm, Table 2.

On the other hand, Fig. 3(a-d) shows the TEM images and their corresponding particle-size distribution histograms (see inset) of the as-synthesized materials. From this figure, a semi-spherical shape of palladium nanoparticles having average sizes from 3.2 to 3.7 nm and good distribution on the carbon support can be observed. According with these results, no significant differences related with morphology and palladium-particle size were observed as a function of the stabilizer. However, the presence of the stabilizer during the synthesis reaction avoids the aggregation and modulates the growth of palladium nanoparticles on the support matrix, the nature and metal:stabilizer ratio can change equilibrium on the surface of the nanoparticles. On the other hand, using energy-dispersive X-ray (EDS) technique, the presence of Pd and C for the as-synthesized materials was confirmed, as expected. The presented values were obtained from the average at three different regions in the sample, Table 2.

3.2. BET isotherm

BET analysis was carried out. According to Fig. 4, the adsorption and desorption isotherms of N$_2$ acquired the shape of type I isotherms, the convex shape of this isotherm is due to the weak interaction between adsorbent and adsorbate. The elevation of the curve near the saturation pressure is a consequence of the adsorption in the micropores (type H3 isotherm), which is associated with aggregates or agglomerations of solids with a homogeneous particle size, controlled by the stabilizer in turn. In Table 1, the values of the specific surface area, pore volume and pore size are summarized. The results reveal that the specific surface

Table 1

Specific surface area, pore volume, and pore size for Pd/lignin/C, Pd/oleylamine/C, Pd/octylamine/C, and Pd/2-methyl-2-butanol/C electrocatalysts.

Catalyst	Specific surface area m^2/g	Pore volume cm^3/g	Pore size Å
Pd/lignin/C	95	0.65	17
Pd/oleylamine/C	44	0.42	15
Pd/octylamine/C	57	0.41	15
Pd/2-methyl-2-butanol/C	55	0.48	17

Table 2
Crystallite and particle size and Pd and C content of the as-synthezized electrocatalysts obtained from XRD, TEM, and SEM-EDS, respectively.

Sample identification	Rietveld refinement XRD			TEM			XPS		
	RWP	Pd crystallite size (nm)	Lattice parameter a (Å)	Particle size by TEM (nm)	TEM lattice fringe distance (nm)	wt% Pd by (EDS-SEM)	wt% Pd by (XPS)	Atomic ratio Pd-C/ (Pd^0 +PdO+PdO$_2$ +PS)	D parameter
Pd/lignin/C	3.94	4.9	3.9188 (6)	3.2 ± 0.5	0.2424	10.33	9.6	0.52	22.02
Pd/oleylamine/C	3.87	5.4	3.9277 (5)	3.7 ± 0.5	0.3845	10.26	9.5	0.49	21.44
Pd/octylamine/C	4.50	3.6	3.9881 (7)	3.3 ± 0.7	0.3755	10.11	9.4	0.34	20.75
Pd/2-methyl-2-butanol/C	–	–	–	3.4 ± 0.5	0.3936	10.22	9.2	0.27	17.52

area can vary depending on the stabilizer. The Pd/lignin/C catalyst exhibits the highest specific surface area, as expected. However, the specific surface area value for the Pd/oleylamine/C catalyst would be expected to follow the trend Pd/lignin/C > Pd/octylamine/C > Pd/2-methyl-2-butanol/C > Pd/oleylamine/C. Nevertheless, this is not the case, and it is suggested that this trend is not followed due to the size of the carbon-chain: for oleylamine this chain is larger than that for octylamine and that for 2-methyl-2-butanol. For this reason, the adsorption-desorption of N$_2$ on the catalyst could be a more tortuous process than with the other catalysts. In this context, the particle size obtained using TEM (see Fig. 3) has a major-proportional effect in the BET area of the catalysts, where the average diameter of the pores was mono-modal in all cases. On the other hand, notice that the average particle-size follows the trend Pd/lignin/C (3.7 ± 0.5 nm) > Pd/octylamine/C (3.4 ± 0.7 nm) > Pd/2-methyl-2-butanol/C (3.2 ± 0.5 nm) > Pd/oleylamine/C (3.2 ± 0.5 nm); whereas the specific surface area follows the order Pd/lignin/C (95 m^2/g) > Pd/octylamine/C (57 m^2/g) > Pd/2-methyl-2-butanol/C (55 m^2/g) > Pd/oleylamine/C (44 m^2/g). Table 3.

Then, linked with these results and according to the test carried out using DEMS (see below), the Pd/octylamine/C sample has a better hydrogen production during the electrocatalytic process with respect to the other catalysts, and was in the order Pd/oleylamine/C > Pd/2-methyl-2-butanol/C > Pd/octylamine/C > Pd/lignin/C.

Following with this analysis, XPS was performed to obtain information on the electronic properties of the materials and their oxidation states. Fig. 5 shows the XPS-general spectra for Pd/lignin/C, Pd/oleylamine/C, Pd/octylamine/C, and Pd/2-methyl-2-butanol/C. The presence of palladium was clearly established and the quantification of the elemental content of C, O and Pd determined (wt%) matches well with the elemental content from EDS-SEM technique, Table 1. The main regions for C1s species can be observed at 284.5 eV, for Pd3d at 340 ± 0.5 eV and for O1s at 531.3 eV.

The oxidation states and chemical species of the electrocatalysts were obtained from the high-resolution spectra corresponding to the regions of Pd3d$_{5/2}$ and Pd3d$_{3/2}$; Table 2 summarizes the deconvolution model for both regions, related with the contribution of the seven chemical species of Pd. In this context, for metallic palladium the corresponding binding energies are located at 335.3 ± 0.2 and 340.70 ± 0.2 eV for Pd3d$_{5/2}$ and Pd3d$_{3/2}$ [51], respectively; see Fig. 6. Whereas, for Pd-C species the corresponding energies were allocated at 336.0 ± 0.2 and 341.2 ± 0.2 eV [52]; these interactions with the carbon-support play an important role during the reduction process, see below. On the other hand, for the case of PdO the corresponding binding energies assigned to (Pd3d$_{5/2}$) and (Pd3d$_{3/2}$) are located at 336.7 ± 0.2 and 342.0 ± 0.2 eV, respectively [53], whereas for PdO$_2$ were 337.4 ± 0.2 and 342.7 ± 0.2 eV [54]. The presence of these two species could be related with oxidation of the main-matrix material during sample preparation XPS analysis in air atmosphere. For Pd^{2+}-species, two satellites were found. The satellite I was localized at 339.1 ± 0.2 eV (for Pd3d$_{5/2}$) and 344.3 ± 0.2 eV (for Pd3d$_{3/2}$) [55]; whereas, the satellite II, assigned to (Pd3d$_{5/2}$) and (Pd3d$_{3/2}$) was allocated at 340.0 ± 0.2 and 345.2 ± 0.2 eV, respectively [54]. Also, the parental species for all

samples corresponding to (Pd3d$_{5/2}$ and Pd3d$_{3/2}$) were allocated at 338.4 ± 0.2 and 343.5 ± 0.2 eV, respectively [56]; these species could be related to the presence of some traces from the organometallic precursor (i.e. Pd(dba)$_2$) employed during synthesis.

Notice that the XPS spectra from Fig. 6 present a shape modification depending on the stabilizer employed, indication of an electronic-surface-material level alteration-modification. In this context, at nanometric-scale induced-electrocatalysis, it has been reported that the electronic properties of actives sites on the material-surface (as well as the dispersion of the metallic nanoparticles on the support) play a crucial role during the charge-transfer process [57].

Thus, in order to understand the effect of the support-matrix employed (e.g., carbon hybridization), and its interaction with the metallic-precursor to induces a catalytic effect in NO$_x$-reduction, Figs. 6 and 7 show an important approach. In Fig. 7 high resolution XPS spectrum of the C1s orbital shown some kind of defects in the intrinsic-structure of the Vulcan carbon support acquired during in-situ synthesis. The FWHM magnitudes and C1s orbital-associated energy for the analyzed samples are organized and showed in Table 4.

From Fig. 7(a-d), it is interesting to note that the maximum position of the main peak is at ca 0.284.5 eV, and a single asymmetrical-narrow peak with a tail toward major energy is also observed; behavior assigned to the presence of C-sp^2 hybridization. In this context, C1s spectra were adjusted from different chemical species and functional groups. For example, C-C bond energies at 283.9 ± 0.2 eV can be attributed to defect zones that could arise from carbon-active vacancies [34]. On the other hand, the signal observed at 284.6 ± 0.2 eV could be assigned with regions containing carbon sp^2 hybridization on the surface or in shallow layers [58]. Whereas C-sp^3 assigned-hybridization can be observed at 285.3 ± 0.2 eV; and with bond-species such as C-OH, C-O-C, C-O, COOHO, π-π *, and (O-C(O)-O) at 258.9 ± 0.2 eV, 287.5 ± 0.2 eV, 288.3 ± 0.2 eV, 289.4 ± 0.2 eV, 290.6 ± 0.2 eV, and 291.7 ± 0.2 eV, respectively [57]. These contributions, as expected, correspond to carbon-atoms signals toward different functional groups that could be attached to the catalyst surface.

From Fig. 7(a-d) the obtained XPS-profiles of the carbonaceous species present a Gaussian-Lorentzian type footprint. In addition, C-sp^2 hybridization-peak exhibits an exponential tail towards higher binding energies, attributed to its high conductivity [58]. The results from C1s spectra and the quantification for each component are summarized in Table 4.

On the other hand, from the Auger C KLL spectra, the carbon hybridization content (sp^2/sp^3) was calculated taking into account the distance (D) between the most positive maximum-peak and the most negative minimum-peak [56], Fig. 8. The value for this D-parameter is 14.2 eV (for diamond) and 22.5 (for graphite). Then, the degree or percentage of hybridization can be compared for carbon-based material between these two limits. In this context, D parameter is highly linked with the atomic-carbon configuration and could be also related to the interaction of other material presented at the carbon-matrix (i.e., palladium nanoparticles) as the surface-state and structure is strongly affected by the sp^3-sp^2 hybridization. The calculated D for the samples in study was 22.02, 21.44, 20.75, and 17.52 for Pd/lignin/C,
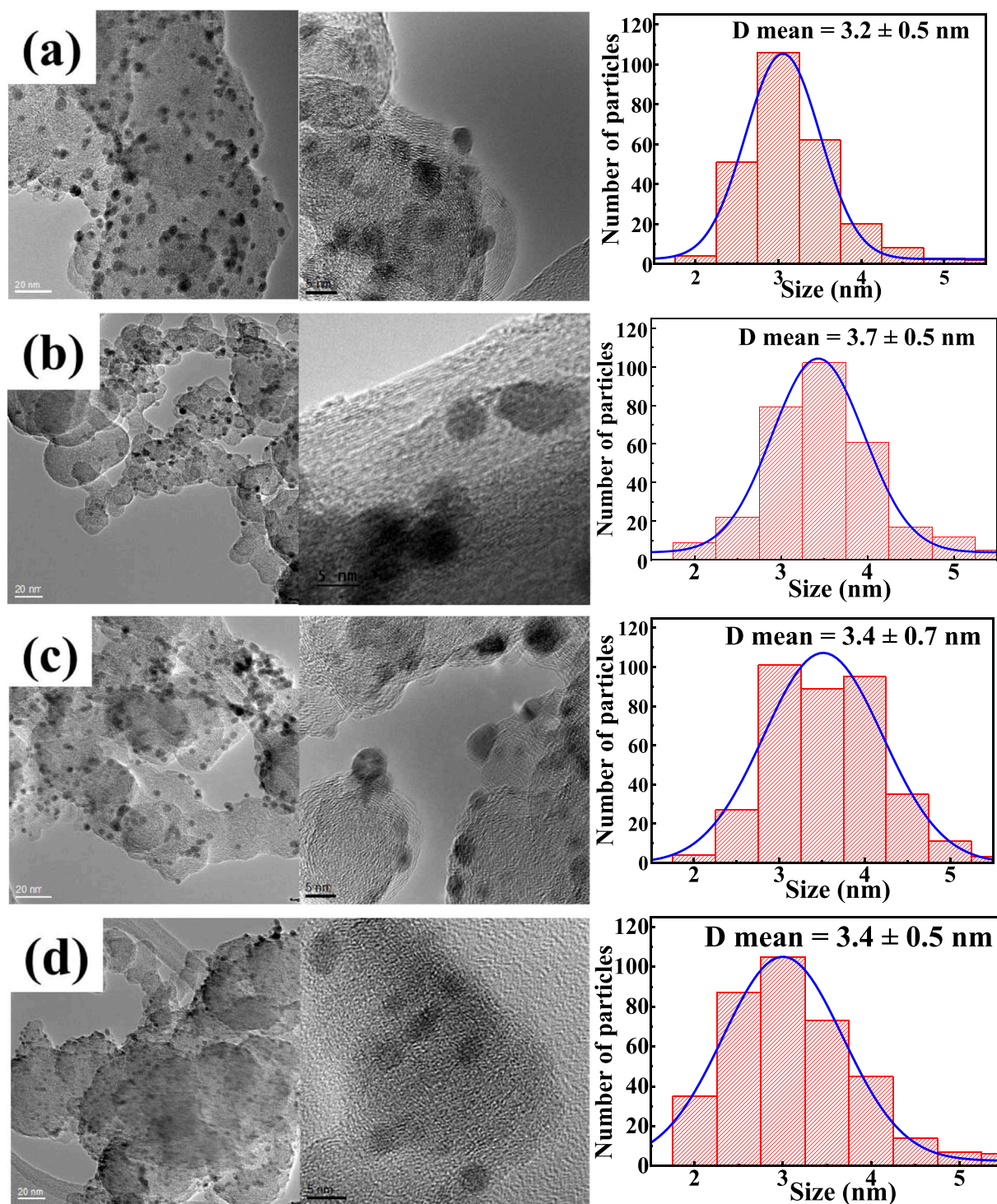
Fig. 3. TEM micrographs and particle-size distribution histograms of (a) Pd/lignin/C, (b) Pd/oleylamine/C, (c) Pd/octylamine/C and (d) Pd/2-methyl-2-butanol/C.

Pd/oleylamine/C, Pd/octylamine/C, and Pd/2-methyl-2-butanol/C, respectively. It is suggested in this work that a higher content of available C-sp^2 sites (given by the stabilizer in turn) the electrochemically active surface area (ECSA) of the material increases significantly, improving the electrochemical reduction of NO_x species.

4. Electrochemical evaluation

4.1. Activation and electrochemical active surface area (ECSA)

Fig. 9 shows the current-potential characteristics obtained using cyclic voltammetry for Pd-base materials (10 % wt. Pd) stabilized with lignin, oleylamine, octylamine, and 2-methyl-2-butanol supported on Vulcan carbon in a potential range from 0.7 to − 0.85 V/RHE. The scan rate was fixed at 20 mVs^{-1} during 30 cycles in a 0.5 M NaOH solution as supporting electrolyte (free of probe molecule), purged with argon prior
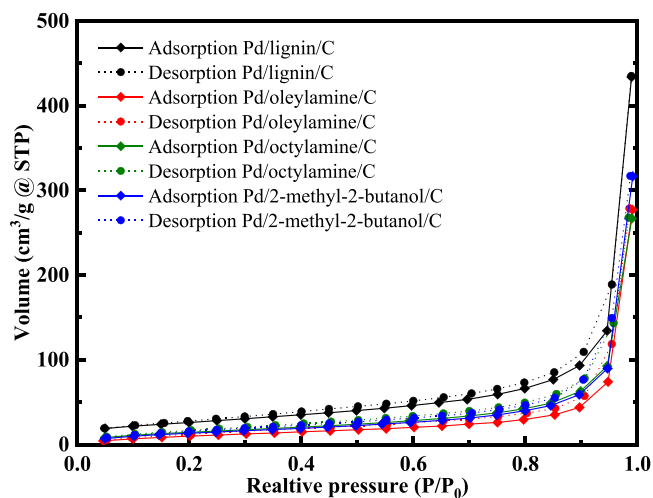
Fig. 4. N$_2$ adsorption/desorption isotherms of Pd/lignin/C, Pd/oleylamine/C, Pd/octylamine/C, Pd/2-methyl-2-butanol/C, and a comparison of these catalysts.

to polarization; after 15 cycles, the current versus potential profiles were stable (surface cleaning, catalyst stability). In Fig. 9, the last cycle is presented. From these profiles it is evident that the stabilizer has an effect in the current intensity, begin more marked in the proton adsorption-desorption zone. In a first approach, notice that the major current in the cathodic zone (from ca. −0.2 to −0.85) is assigned to the catalyst stabilized with lignin. Moreover, the current increases, within experimental error, in the order Pd/lignin/C > Pd/oleylamine/C > Pd/octylamine/C > Pd/2-methyl-2-butanol/C during protons adsorption (in the interval from ca. −0.6 to −0.85 V/RHE, negative-going scan) and protons desorption (in the interval from −0.5 to −0.25, positive-going scan); related with the ECSA. These results could be linked with the D-

parameter, increasing in the order Pd/lignin/C (22.02) > Pd/oleyl-amine/C (21.44) > Pd/octylamine/C (20.75) > Pd/2-methyl-2-butanol/C (17.52); as more electronic-support contributions (e.g., major conductivity and C-sp^2 sites) concomitant with the presence of palladium might increases the charge-transfer process at the electrode-electrolyte interface enhancing the catalytic activity.

To verify the assumptions discussed above concerning the relationship between D and the stabilizer in turn, ECSA was calculated for the materials in study. In this context, cyclic voltammetry of the Pd/stabilizer/C electro-catalysts was performed by means of the formation of a complete monolayer of PdO from the anodic charge associated with the desorption peaks of protons adsorbed in the cathodic zone in a one-to-
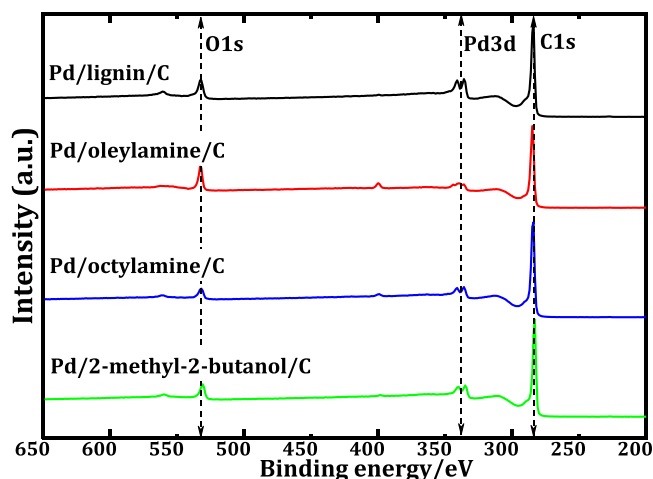

Fig. 5. General XPS spectra for Pd/lignin/C, Pd/oleylamine/C, Pd/octylamine/C, and Pd/2-methyl-2-butanol/C; the main regions for C1s, O1s and Pd3d are observed.

Table 3

Quantification of C, O and Pd species in Pd/stabilizer/C materials from XPS analysis. Link energy (eV) and percentage by weight of the total area of the orbitals Pd3d$_{5/2}$ and Pd3d$_{3/2}$; set of species for Pd: Pd^0, Pd-C, PdO$_2$, PdO, Pd^{2+} and parental species are also shown.

| Chemical species		Pd/lignin/C			Pd/oleylamine/C			Pd/octylamine/C			Pd/2-methyl-2-butanol/C		
		BE [$\pm$ 0.15 eV]	FWHM	wt %	BE [$\pm$ 0.15 eV]	FWHM	wt %	BE [$\pm$ 0.15 eV]	FWHM	wt %	BE [$\pm$ 0.15 eV]	FWHM	wt %
Pd^0	Pd3d$_{5/2}$	335.30	0.89	1.1	335.25	0.96	5.6	335.40	1.00	11.4	335.50	0.90	21.2
	Pd3d$_{3/2}$	340.55	0.89	–	340.70	0.96	–	340.65	1.00	–	340.79	0.90	–
Pd-C	Pd3d$_{5/2}$	335.97	0.91	34.2	336.10	0.96	32.9	336.06	1.06	25.2	336.10	0.95	22.4
	Pd3d$_{3/2}$	341.23	0.91	–	341.35	0.96	–	341.28	1.06	–	341.39	0.95	–
PdO	Pd3d$_{5/2}$	336.58	0.95	30.6	336.87	1.02	30.4	336.60	1.06	36.0	336.60	0.98	22.2
	Pd3d$_{3/2}$	341.87	0.95	–	342.12	1.02	–	341.89	1.06	–	341.88	0.98	–
PdO$_2$	Pd3d$_{5/2}$	337.32	1.09	19.7	337.54	1.15	17.0	337.33	1.17	14.3	337.33	1.09	16.7
	Pd3d$_{3/2}$	342.58	1.09	–	342.87	1.15	–	342.68	1.17	–	342.64	1.09	–
Sat I Pd^{2+}	Pd3d$_{5/2}$	338.96	1.05	–	339.39	1.10	–	339.13	1.12	–	339.20	1.04	–
	Pd3d$_{3/2}$	344.11	1.05	–	344.59	1.10	–	344.45	1.12	–	344.53	1.04	–
Sat II Pd^{2+}	Pd3d$_{5/2}$	339.97	1.25	–	339.97	1.14	–	340.08	1.27	–	340.08	1.20	–
	Pd3d$_{3/2}$	345.10	1.25	–	345.32	1.14	–	345.43	1.27	–	345.43	1.20	–
Parental species	Pd3d$_{5/2}$	338.16	1.13	14.3	338.60	1.21	14.2	338.35	1.21	13.2	338.35	1.15	17.6
	Pd3d$_{3/2}$	343.33	1.13	–	343.80	1.21	–	343.52	1.21	–	343.56	1.15	–
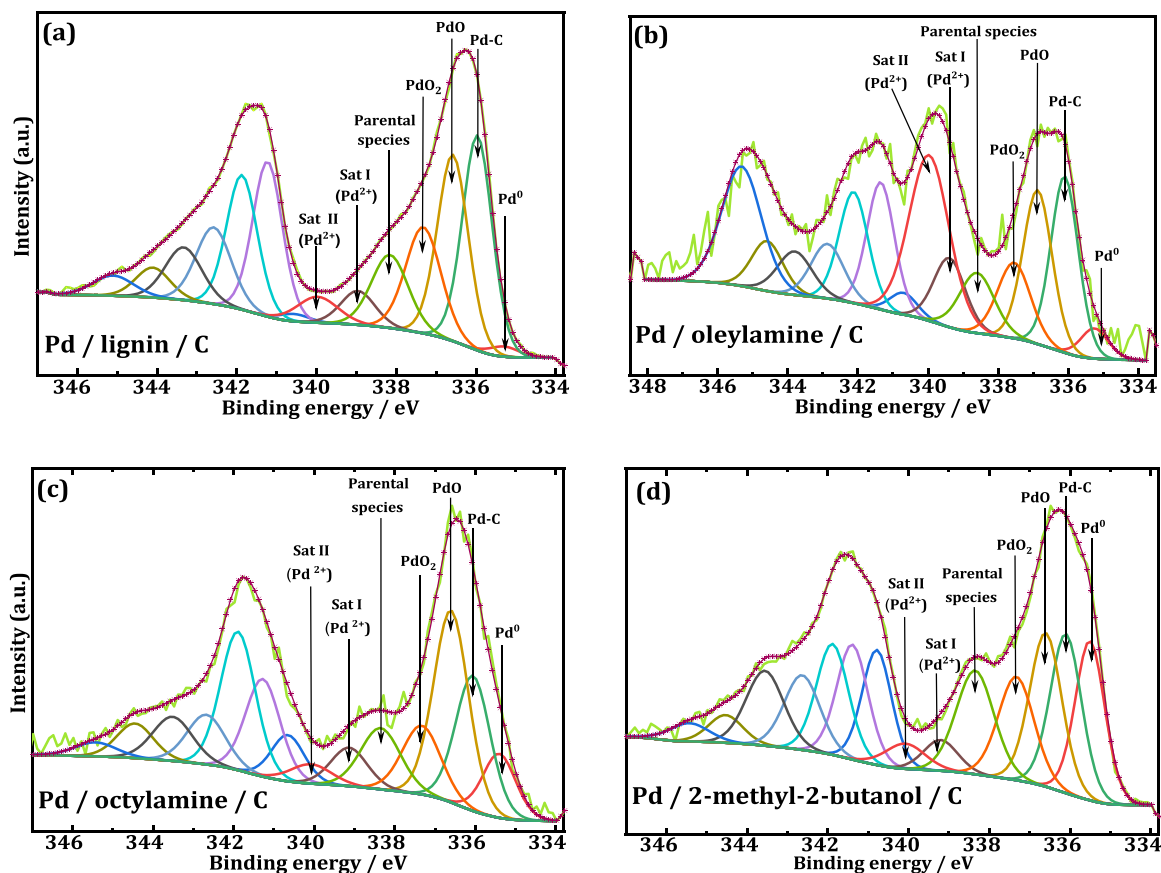
Fig. 6. High-resolution spectra and deconvolution for the synthesized materials from different stabilizers (a) Pd/lignin/C, (b) Pd/oleylamine/C, (c) Pd/octylamine/C, and (d) Pd/2-methyl-2-butanol/C. The spectra are fitted with the main $Pd3d_{5/2}$, orbitals and the set of Pd species: Pd^0, $Pd3d_{3/2}$, Pd-C, PdO, PdO_2; and parental species.

one ratio with respect to Pd atoms at the electrode surface. The obtained profiles related with the redox process of the samples as a function of the switching potential area show in Fig. 10. The Q_{PdO} was calculated taking into account the PdO reduction region according to Eq. (3) [60].

$$Q_{PdO} = \frac{1}{v} \int_{E_i}^{E_f} i(E)dE \qquad (3)$$

Where E_i and E_f are the initial and final potentials at the reduction zone in a PdO_{red} monolayer from -0.262–0.136 V/RHE, respectively. Then, using Eq. (4), ECSA was evaluated assuming a correction of the double layer $S = 420$ m C cm^{-2} [61].

$$ECSA_{PdO}(m^2g^{-1}) = \left[\frac{Q_{PdO} \quad (C)}{S(\mu C \quad cm^{-2} \bullet l \quad (mg))} \right] \bullet 10^5 \qquad (4)$$

Where Q_{PdO} is the charge (C), S is a conversion factor relating the electric charge and the surface area (mC cm^{-2}), and l is the nominal load of palladium in the electrode (mg). Then, ECSA can be obtained by modulating the formation of a PdO monolayer, inducing redox process associated with chemisorbed oxygen-ad-atoms in the monoatomic-surface layer of palladium-species sites [62], [63]. From combination of Eqs. (3–4), the plots in the insets in Fig. 10 were obtained, and the intersection of the slopes generated as a function of the applied potential in the positive-going scan, gives ECSA, being in the order 129.38 (Pd/lignin/C) > 121.95 (Pd/oleylamine/C) > 72.20 (Pd/octylamine/C) > 58.45 (Pd/2-methyl-2-butanol/C); in m^{2}g^{-1}.

Based on these results, it is evident that ECSA and HER-magnitude are linked with the D-parameter throughout the stabilizer. As mentioned, hybridization favored the generation of active Pd sites. Thus, being able to control these properties could be decisive to improve

surface characteristics, as well as selectivity towards desired products such as in the electrochemical reduction of nitrate species.

4.2. NO_x Electro-reduction process and HER

In Figs. 11 and 12, the current versus potential characteristics for the materials in study with respect to stabilizer and nitrate-species nature, is plotted. In a first approach, significant differences in current intensity were observed during the reduction of NO_3^- and NO_2^- with and without $NO_{2(g)}$, depending on the stabilizer in turn. Notice that the redox process in the cathodic side can be assigned to the reduction of nitrates species, as in the supporting electrolyte the observed peaks are linked with the adsorption-desorption of protons (H_{upd} zone), see Fig. 9. In addition, the major faradic current for the reduction process is assigned to the catalyst prepared with lignin as stabilizer, and with D = 22.02.

Jacintó Sá et al., have proposed a possible mechanism for the reduction reaction of nitrides species, which involves adsorption of nitrate at an active site, reduction to nitrite, desorption in the aqueous phase and reabsorption in a mono-metallic site (only at noble metals) where such as species are reduced to final products [64]. In a mono-metallic catalyst, it is believed that the initial step is performed at the active sites of the support and that the selectivity of the products is determined during the final electrochemical reduction reaction stage of the adsorbed nitric oxide ($NO_{(ad)}$). In Fig. 10 (a-b), the i-E profiles have peaks during the negative-going scan that might be related to the electrochemical reduction of NO_3^- ions. In this context, NO_3^{2-} (ad) was reported as intermediate specie during the electrochemical reduction reaction in the alkaline environment [32]; following a sequence in the order electrochemical-chemical-electrochemical (E-C-E) mechanism, as observed in Eqs. (5–7) [26]. In fact, this set of reactions determines the
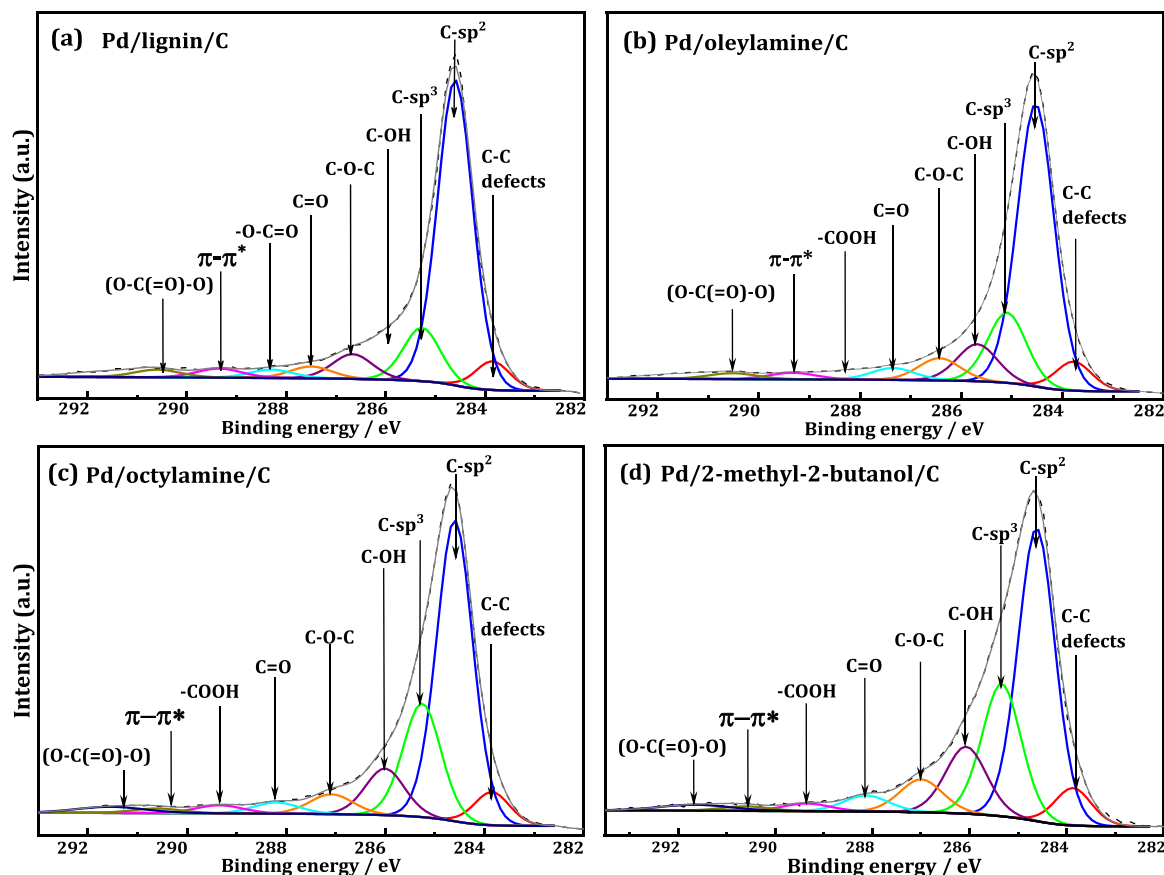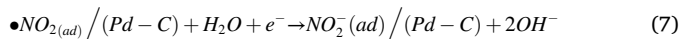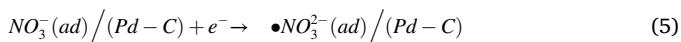
Fig. 7. High-resolution spectra and deconvolution for (a) Pd/lignin/C, (b) Pd/oleylamine/C, (c) Pd/octylamine/C, and (d) Pd/2-methyl-2-butanol/C. The spectra are fitted with the main C1s orbitals and with the set of C species: C-C defects, C-sp^2, C-sp^3, C-OH, C-O-C, C=O, -COOH, π-π * and (O-C(=O)-O).

Table 4

Quantification of C, O, and Pd species in Pd/stabilizer/C materials from XPS analysis. Binding energy (eV) and percentage by weight of the total area of the orbitals Pd3d$_{5/2}$ and Pd3d$_{3/2}$ and the set of species for Pd: Pd^0, Pd-C, PdO$_2$, PdO, Pd^{2+} (and parental species); are also presented.

Chemical species		Pd/lignin/C			Pd/oleylamine/C			Pd/octylamine/C			Pd/2-methyl-2-butanol/C		
		BE [± 0.15 eV]	FWHM	wt %	BE [± 0.15 eV]	FWHM	wt %	BE [± 0.15 eV]	FWHM	wt %	BE [± 0.15 eV]	FWHM	wt %
C-C (Defects)	C1s	283.9	0.85	6.0	283.8	0.87	6.3	283.9	0.87	5.8	283.9	0.93	5.9
C-sp^2	C1s	284.6	0.90	59.9	284.5	0.90	57.0	284.6	0.90	52.2	284.6	0.90	46.6
C-sp^3	C1s	285.3	0.91	11.5	285.1	0.93	15.3	285.3	0.93	20.7	285.3	0.99	22.2
C-OH	C1s	285.9	0.95	8.3	285.7	0.97	8.7	286.0	0.97	8.9	286.1	1.04	11.8
C-O, C-O-C	C1s	287.5	1.03	3.3	287.4	1.05	3.4	287.1	1.07	4.3	287.0	1.09	6.1
C=O	C1s	288.3	1.07	2.9	288.3	1.09	2.5	288.2	1.12	2.6	288.1	1.14	3.2
-COOH, -O-C=O	C1s	289.4	1.11	2.9	289.3	1.13	2.4	289.4	1.16	2.1	289.4	1.18	1.5
π-π*	C1s	290.6	1.15	2.6	290.5	1.17	2.3	290.6	1.20	1.2	290.6	1.20	0.9
(O-C(=O)-O)	C1s	291.7	1.80	2.6	291.6	1.80	2.1	291.6	1.70	2.2	291.1	1.80	1.8

electro-kinetics of nitrate-to-nitrite reduction process [65].

$$NO_3^- (ad) \big/ (Pd-C) + e^- \rightarrow \quad \bullet NO_3^{-} (ad) \big/ (Pd-C) \quad (5)$$

$$\bullet NO_3^{2-} (ad) \big/ (Pd-C) + H_2O \quad \rightarrow \quad \bullet NO_{2(ad)} \big/ (Pd-C) + 2OH^- \quad (6)$$

$$\bullet NO_{2(ad)} \big/ (Pd-C) + H_2O + e^- \rightarrow NO_2^- (ad) \big/ (Pd-C) + 2OH^- \quad (7)$$

On the other hand, as in the case of NO$_3^-$, in Fig. 12 profiles associated to the reduction of nitrites (a) and nitrites + NO$_{2(g)}$ (b), are plotted. For instance, such profiles are quite different to those obtained with nitrates (and NO$_{2(g)}$) as expected, see Fig. 10.

The obtained current-versus-potential characteristics at different

stabilizer could be linked with a charge-transfer process to form a radical di-anion NO$_2^{2-}$ Eq. (8), followed by an hydrolysis reaction forming NO$_{(ads)}$, Eq. (9) [66]. Moreover, as in the case of Figs. 11–12, the faradic current increases, within experimental error, in the order of the stabilizer in turn and with the D-parameter: Pd/lignin/C > Pd/oleylamine/C > Pd/octylamine/C > Pd/2-methyl-2-butanol/C (in the interval from ca. −0.6 to −0.85 V/RHE, during the negative-going scan).

Therefore, during the electrochemical reduction of NO$_2^-$, intermediate NO reacts with H$_{(ad)}$ forming adsorbed species. This step can modulates the selectivity and conversion during reduction of NO; initiating with NO adsorption at active Pd-C sites, followed by an electrochemical-electrochemical (E-E) process carried out throughout a charger-transfer reaction [67].
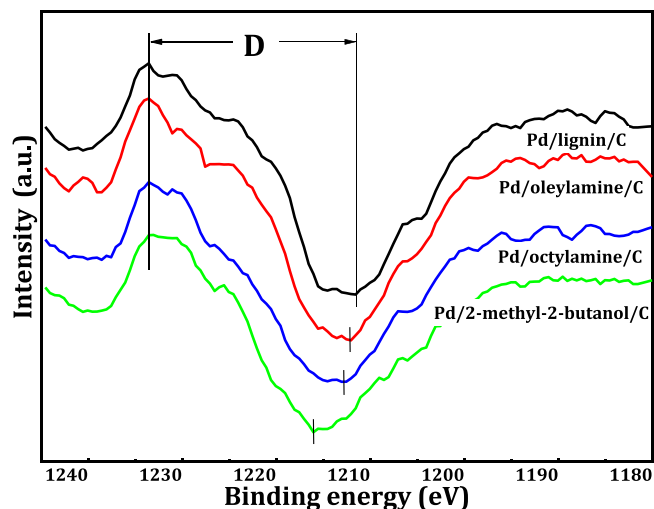
Fig. 8. Derivative of C KLL spectra for Pd/lignin/C, Pd/oleylamine/C, Pd/octylamine/C and Pd/2-methyl-2-butanol/C, from which the parameter D was estimated using the analysis of Lascovich et al. [59].
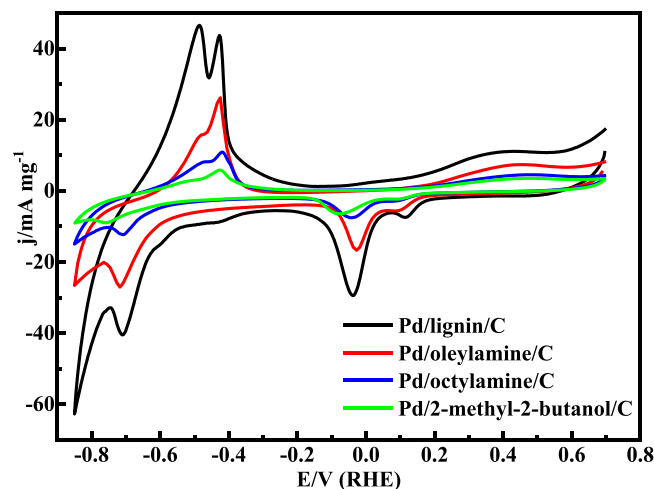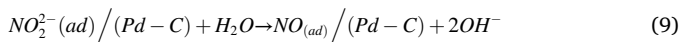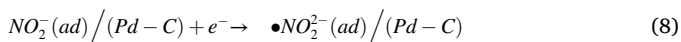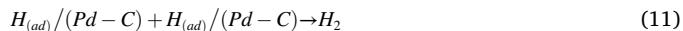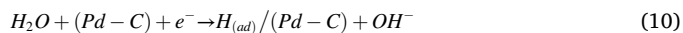

Fig. 9. i-E profiles of Pd/lignin/C, Pd/oleylamine/C, Pd/octylamine/C and Pd/2-methyl-2-butanol/C in NaOH (0.5 M) solution. Scan rate of 20 mVs^{-1}.

$$NO_2^- (ad) \Big/ (Pd - C) + e^- \rightarrow \quad \bullet NO_2^{2-} (ad) \Big/ (Pd - C) \tag{8}$$

$$NO_2^{2-} (ad) \Big/ (Pd - C) + H_2O \rightarrow NO_{(ad)} \Big/ (Pd - C) + 2OH^- \tag{9}$$

According with literature, the NO could be adsorbed in the active sites of noble metal and also in the support employed. Therefore, the reaction kinetic could be influenced by species adsorbed on the support-matrix side. In our study, for example, the electronic-interaction at the couple active-metal/support-matrix is altered for the stabilizer employed during material preparation, as demonstrated form XPS analysis.

Also notice that, for the same stabilizer, the hydrogen evolution reaction (HER) presents different behavior-current-magnitude, Fig. 13 (a-d); liked with the anion in turn and the presence of NO$_{2(g)}$. For all cases, the faradic current associated with the HER, shifts to more positive potentials at solutions based in nitrogen ions, being more marked during reduction of NO$_2^-$ + NO$_{2(g)}$. Therefore, in a parallel mechanism, protons are adsorbed (H$_{(ad)}$) at active Pd-C sites, according to Eq. (10) [64]. Thereafter, from the recombination of H$_{(ad)}$, at more negative potential, the HER takes place, Eq. (11).

$$H_2O + (Pd - C) + e^- \rightarrow H_{(ad)} \Big/ (Pd - C) + OH^- \tag{10}$$

$$H_{(ad)} \Big/ (Pd - C) + H_{(ad)} \Big/ (Pd - C) \rightarrow H_2 \tag{11}$$

4.3. Impedance analysis

Electrochemical impedance spectrometry was carried out during theNO$_2^-$ electroreduction reaction for the catalysts Pd/lignin/C, Pd/oleylamine/C, Pd/octylamine/C, and Pd/2-methyl-2-butanol. Frequency intervals from 100,000–0.01 Hz at − 0.65 V, and an amplitude of 0.01 V. The corresponding Nyquist plots are presented in Fig. 14. The characteristics follow a quasi-semicircular shape indicating a capacitive behavior during charge transfer interfacial-redox reactions. Nevertheless, the resulting RCT increases depending on the stabilizer in turn during cathodic polarization, increasing the number of resistors and processes for charge transfer. These data were fitted by a proposed equivalent electric circuit using the EC-Lab software and displayed as a solid line in Fig. 14. It is important to note that the impedance values are larger for Pd/oleylamine/C and Pd/octylamine/C during polarization at − 0.65 V/RHE, as expected. Conversely, depending on the resistive contribution for each catalyst to high frequencies it is possible to distinguish that the impedance values increase four or two orders of magnitude are observed with respect to Pd/lignin/C and Pd/2-methyl-2-butabol/C at the applied potential (see Fig. 14). To further analyze the electrochemical nature of each Pd base catalyst in the reduction of nitrate species, the circuits for Pd/lignin/C and Pd/2-methyl-2-butanol/C, Pd/oleylamine/C, and Pd/octylamine/C, were obtained from the simulation of the EIS diagrams, see insets in Fig. 14.

The equivalent circuits considered the following contributions. First, for the four electrocatalysts, R1 is related to the resistance of the electrolyte and W4 can be related with the desorption of the electroreduction products. Furthermore, for Pd/lignin/C and Pd/2-methyl-2-butanol/C, the array Q1/C2 +R2 can be related to a simultaneous adsorption-reaction process at the electrode-electrolyte interface during the reduction process. On the other hand, for the Pd/oleylamine/C, and Pd/octylamine/C catalysts, the arrangements C2 / R3 +W3 and C2 +R2 / R3 +W3 can be related to adsorption-desorption processes of the reactants and products generated during the redox reaction, respectively. The element RCT could be related to the kinetic of the interfacial charge-transfer reaction and increases with the sp2 hybridization concentration. Therefore, higher content of sp2 hybridization might enhance the electron mobility by decreasing the recombination of electron-hole pair. These results indicate that the nature of each material can be selective, improving or increasing charge and mass transfer processes depending on the stabilizer in turn. It is assumed that the electroreduction on these catalysts depends on several aspects, such as i) the size of the metal nanoparticles, ii) the chemical composition, iii) the crystal structure, and morphology (related with the concentration of sp2 sites) and iv) the interaction of the active sites (metal nanoparticles) of the catalysts with the carbon Vulcan support.

5. In-situ detection using DEMS

In-situ detection of species generated at the electrode interface was carried out using DEMS technique. Simultaneously, during the electrochemical reduction of NO$_2^-$ +NO$_{2(gas)}$ (faradic current, i$_f$), (m/z) ratios linked with ionic current (i$_i$) were recorded in a potential window from 0.7 to − 0.85 V/RHE using cyclic voltammetry at scan rate of 2 mVs^{-1}. The electrode employed was the most active for the reduction in turn: Pd/lignin/C.

Same experiments were carried out in the supporting electrolyte (0.5 M NaOH) free of NOx-species; the recorded mass signals were NH$_3$ (m/z = 17), N$_2$H$_4$ (m/z = 32), N$_2$O (m/z = 44), N$_2$ (m/z = 28), and H$_2$ (m/z = 2). Fig. 15 resume the obtained results. A first inspection in Fig. 15 put in clear that in absence of nitrate species (i.e., NO$_2^-$ and NO$_2$
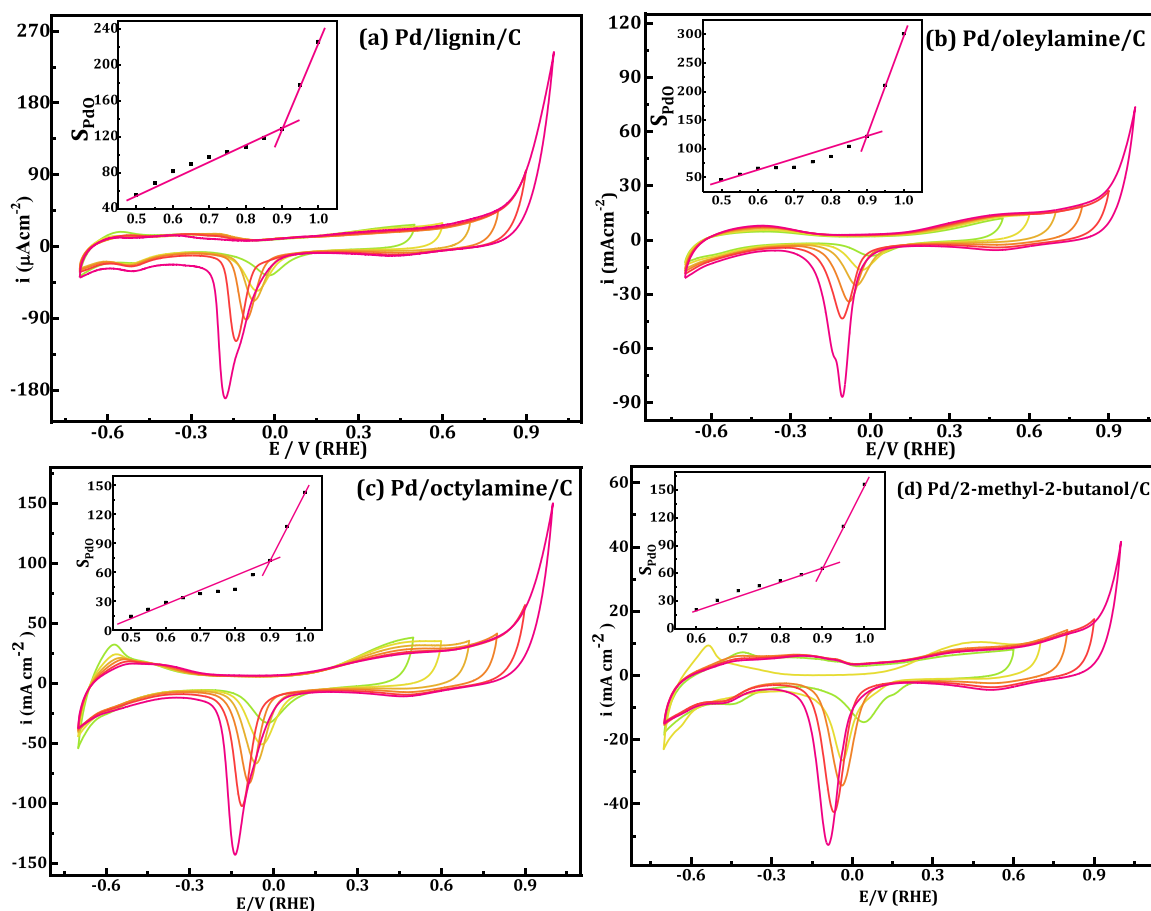
Fig. 10. Profiles for the calculation of the electrochemical active area for (a) Pd/lignin/C, (b) Pd/oleylamine/C, (c) Pd/octylamine/C, and (d) Pd/2-methyl-2butanol/C electrocatalysts. The insets represent the charge for reduction of the oxides formed during the anodic scan as a function of the shifted-applied potential.
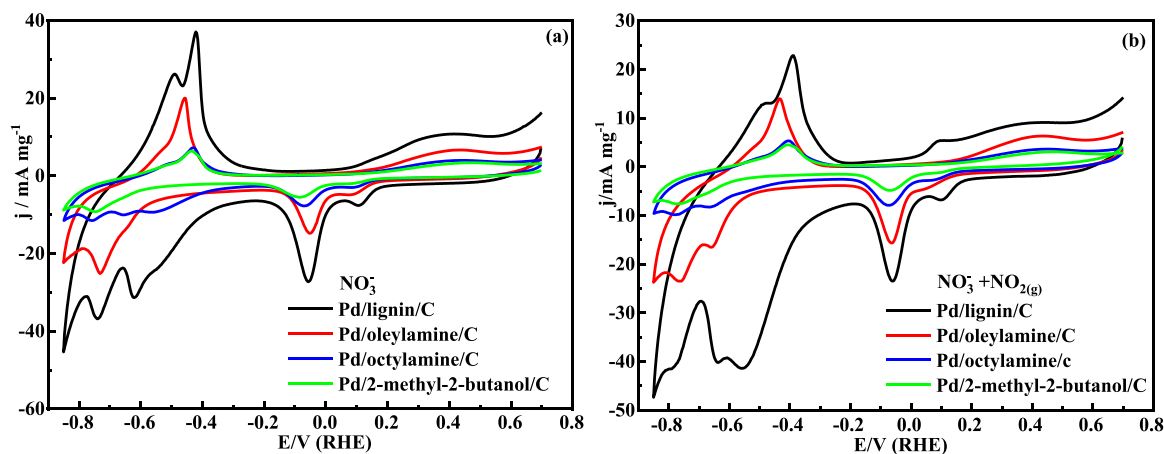

Fig. 11. i-E profiles in alkaline conditions for Pd/lignin/C, Pd/oleylamine/C, Pd/octylamine/C and Pd/2-methyl-2-butanol/C; (a) NO_3^-, and (b) $NO_3^- + NO_2$ at NaOH (0.5 M) solution. Scan rate of 20 mVs^{-1}.

(g)) the faradic current generated at the electrode during cathodic polarization (Fig. 15a) induces the production of molecular hydrogen ($m/z = 2$, Fig. 15b); whereas, ionic current for species such as N$_2$ ($m/z = 28$), N$_2$O ($m/z = 44$), N$_2$H$_4$ ($m/z = 32$), and NH$_3$ ($m/z = 17$), Fig. 15 c-g, respectively; were not detected with DEMS, as expected. Conversely, at solution containing NO$_x$-species, the assigned faradic-current (Fig. 15 h) is more marked than that in solution free of NO$_x$ (cf. Fig. 15a). Consequently, the ionic current assigned to molecular nitrogen, N$^+$, N$_2$O, N$_2$H$_4$ and ammonia, Fig. 15j-n, were detected with DEMS.

It is interesting to note that (i) molecular hydrogen was also detected (Fig. 15i); however, the ionic-current magnitude (ca. 2×10^{-12} A) is similar to that obtained at solution free of NO$_x$-species (cf. Fig. 15b), and (ii) an onset to more negative potential for the production of hydrogen (Fig. 15i) is observed with respect to the generated-nitrogen species; indication that a major amount of protons are adsorbed at the electrode interface, modulating the selectivity and conversion toward NO$_x$-species. In this context, the pumped electrons from the external-energy source also controls the reaction kinetic; delaying the HER (available
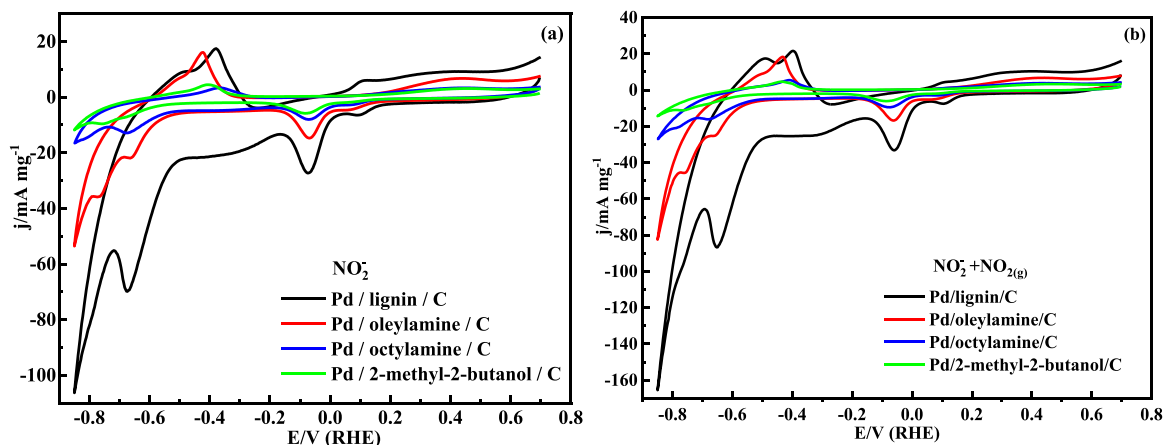
Fig. 12. i-E profile in alkaline conditions for Pd/lignin/C, Pd/oleylamine/C, Pd/octylamine/C, and Pd/2-methyl-2-butanol/C; (a) NO_2^-, and (b) $NO_2^- + NO_{2(g)}$ at NaOH (0.5 M) solution. Scan rate of 20 mVs^{-1}.
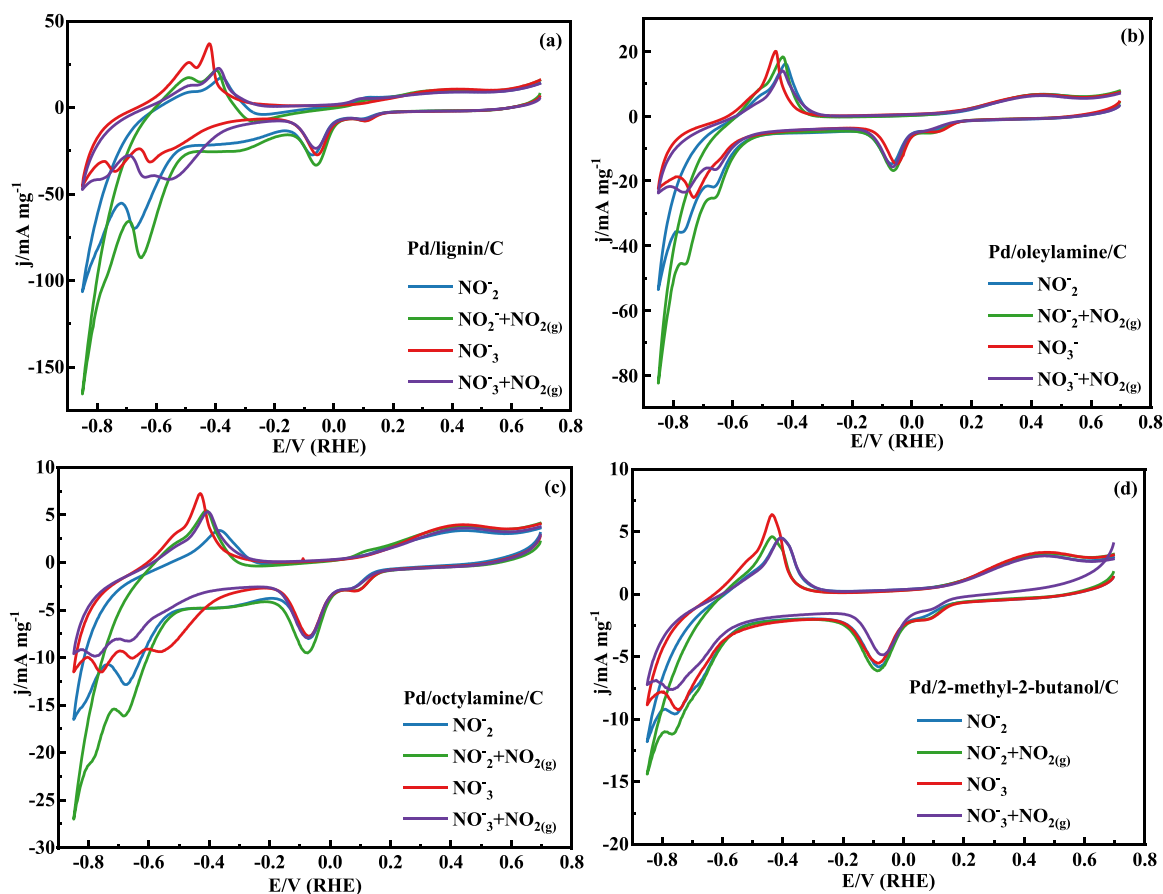

Fig. 13. i-E profiles obtained during the electro-reduction of nitrate and nitrite in presence of nitrogen dioxide as a function of stabilizer (a) lignin, (b) oleylamine, (c) octylamine, and (d) 2-methyl-2-butanol. Solution of NaOH (0.5 M). Scan rate of 20 mVs^{-1}.

adsorbed-active-site protons), due to the intrinsic properties of the material in turn as discussed above (cf. XRD and XPS sections). Similar results concerning the formed species were reported elsewhere [26]. On the other hand, the mass signal ($m/z = 14$, Fig. 15), attributed to the fragment N$^+$, confirms the generation of molecular nitrogen. From these results, an important step in the reduction reaction is the conversion of nitrates to nitrites (Eqs. 5–7). Thereafter, the formation of NO (Eqs. 8–9) throughout the reduction of adsorbed nitrites is possible, as the adsorbed-protons interact with nitrites-ions (Eq. 10) [68]. In this step, the intrinsic nature of the material employed modulates-shifts the HER

toward more negative potentials (see also inset in Fig. 16A). Then, the presence of H$_{(ad)}$ could promotes the formation of N-H bonds, and/or N-N, species [69].

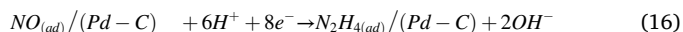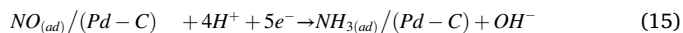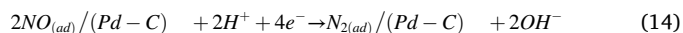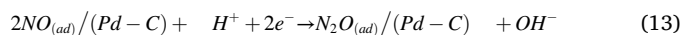As mentioned, the adsorbed nitrogen monoxide $NO_{(ad)}/(Pd-C)$ (Eq. (12)), could promotes the generation of some species (depending on several conditions as pH, probe-molecule concentration, supporting-electrolyte nature, applied potential, surface state, among other) such as N$_2$O, N$_2$, NH$_3$, and N$_2$H$_4$, Eqs. (13–16) [70] and Fig. 15.

$$NO + (Pd-C) \rightarrow NO_{(ad)}/(Pd-C) \tag{12}$$
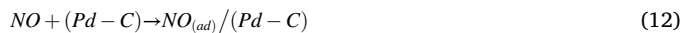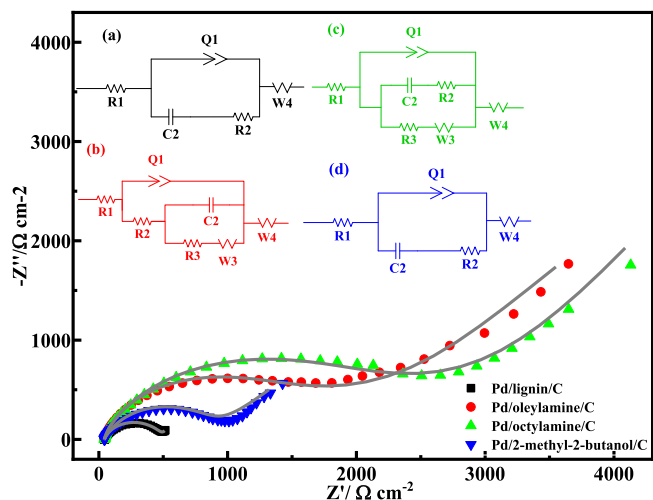
Fig. 14. Nyquist plots representation with its corresponding fitting of the − 0.65 V. Equivalent circuits used for the fitting of the EIS diagrams of (a) Pd/lignin/C, (b) Pd/oleylamine/C, (c) Pd/octylamine/C, and (d) Pd/2-methyl-2butanol/C electrocatalysts. The experimental data are represented by discrete points, and the simulation impedance response is represented by a continuous line.

$$2NO_{(ad)}/(Pd-C)+ \quad H^+ + 2e^- \rightarrow N_2O_{(ad)}/(Pd-C) \quad +OH^- \tag{13}$$

$$2NO_{(ad)}/(Pd-C) \quad +2H^+ + 4e^- \rightarrow N_{2(ad)}/(Pd-C) \quad +2OH^- \tag{14}$$

$$NO_{(ad)}/(Pd-C) \quad +4H^+ + 5e^- \rightarrow NH_{3(ad)}/(Pd-C)+OH^- \tag{15}$$

$$NO_{(ad)}/(Pd-C) \quad +6H^+ + 8e^- \rightarrow N_2H_{4(ad)}/(Pd-C)+2OH^- \tag{16}$$

Then, DEMS analysis permits an approach for the study of reaction mechanism as in the case presented in this investigation. In addition, from the faradic-current versus ionic-current plot, a qualitative comparation related with the nitrogen-based generated species and HER could be done, Fig. 16 [32].

Interestingly, notice that HER reaction is clearly inhibited in the presence of $NO_2^- + NO_{2(g)}$, Fig. 16B (and inset in Fig. 16A); promoting the formation of the species mentioned above. It is worth to mention that in solution free of probe molecule, the only specie produced is hydrogen, as observed in Fig. 16A.

These results put in evidence that the interaction between protons in alkaline environment and surface properties of the actives sites at Pd/lignin/C electro-catalyst might modify the selectivity towards selected species. For this case of study, the proposed pathway is presented in Schema 1.

$$NO_3^-(ad) \rightarrow NO_2^-(ad) \rightarrow NO_{(ad)} \quad \rightarrow \begin{Bmatrix} N_2O \\ N_2 \\ NH_3 \\ N_2H_4 \end{Bmatrix}$$
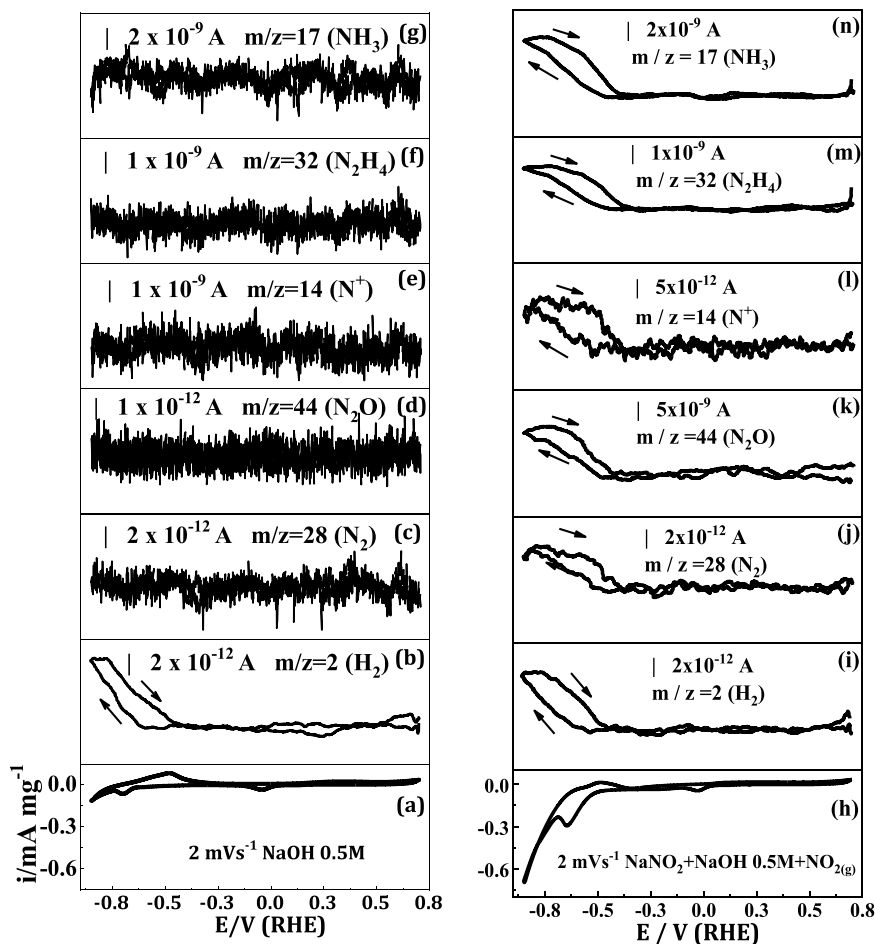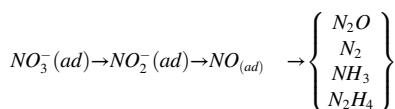
Fig. 15. i-E characteristics during cathodic polarization at Pd/lignin/C electrode in (a) NaOH 0.5 M, and (h) NaNO$_2$ + NaOH 0.5 M saturated with NO$_{2(g)}$. Mass signal (ionic-current) vs potential obtained using DEMS for (b, i) H$_2$, (c, j) N$_2$, (d, k) N$_2$O, (e, l) N$^+$, (f, m) N$_2$H$_4$, and (g, n) NH$_3$. Scan rate of 2 mVs^{-1}.
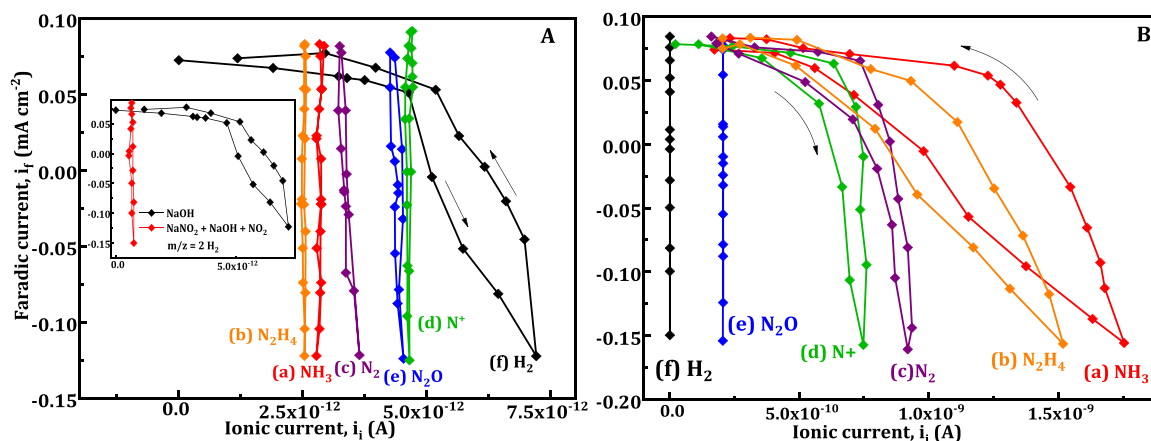
Fig. 16. Ionic-current (i_i) vs faradic-current (i_f) profiles from mass-intensity and potentiostatic-current signals. (a) NH_3, (b) N_2H_4, (c) N_2, (d) N^+, (e) N_2O, and (f) H_2. Data obtained from Fig. 14. Inset: (i_i) vs (i_f) during the hydrogen evolution reaction (HER).

Schema 1. Reaction sequence obtained for the reduction of nitrates species using DEMS.

Therefore, as confirmed in this work, modulating the presence of C-sp^2 sites during synthesis (caused by the stabilizer in turn) also changes the interaction support-noble metal and the selectivity-conversion during the electrochemical process. The major impact was observed in the adsorption-desorption process of protons and, eventually, in the HER at more negative potentials.

6. Conclusions

Nanostructured palladium stabilized with lignin, oleylamine, octylamine, or 2-methyl-2-butanol materials were synthesized from $Pd(dba)_2$ precursor using the ligands-displacement of organometallic precursors methodology. From XRD and TEM results, no significant differences related with structure, morphology and palladium-particle size were observed as a function of the stabilizer, confirming that its presence during synthesis reaction avoids the agglomeration and modulates the growth of palladium nanoparticles on the support matrix. In the case of XPS, as shape modification in the binding energy characteristics was observed depending on the stabilizer employed (possible indication of an electronic-surface-material modification) inducing an important electrocatalytic effect during charge-transfer process. In addition, the calculated D-parameter for the samples in study was 22.02, 21.44, 20.75 and 17.52 for Pd/lignin/C, Pd/oleylamine/C, Pd/octylamine/C, and Pd/2-methyl-2-butanol/C, respectively; indicating that at higher content of available C-sp^2 sites, the ECSA is modified in the order 129.38 (lignin) > 121.95 (oleylamine) > 72.20 (octylamine) > 58.42 (2-methyl-2-butanol) m^2g^{-1}. This modification improves the electrochemical reduction of NO_x species for the catalyst stabilized with lignin. In this context, during cathodic polarization species such as NH_3, N_2H_4, N_2O, and N_2 were observed using DEMS with HER ($m/z = 2$) at more negative potentials. Therefore, adsorbed protons at the electrode interface could modulate the selectivity and conversion toward less contaminant spices (i.e., N_2, N_2O) and/or commercial interest compounds (i.e., N_2H_4, NH_3) as also demonstrated from the faradic-current (i_f) versus ionic-current (i_i) characteristics in a real-time detection using mass spectroscopy.

CRediT authorship contribution statement

S. Vázquez-Bautista: Investigation, Writing - original draft, Methodology, Formal analysis **G. Zacahua-Tlacuatl**: Formal analysis, Writing - review & editing. **A. Manzo-Robledo**: Conceptualization, Methodology, Formal analysis, Resources, Writing - review & editing, Funding acquisition. **E. Ramírez-Meneses**: Conceptualization,

Methodology, Formal analysis, Resources, Writing - review & editing, Funding acquisition.**J. Acosta-Jara, L. Pedraza-Segura, M. Luna-Trujillo and L. Lartundo-Rojas**: Investigation, Methodology.

Declaration of Competing Interest

The authors declare that they have no known competing financial interests or personal relationships that could have appeared to influence the work reported in this paper.

Data availability

Data will be made available on request.

References

[1] M. Kampa, E. Castanas, Human health effects of air pollution, Environ. Pollut. 151 (2) (2008) 362–367, https://doi.org/10.1016/j.envpol.2007.06.012.

[2] C.R. Jacobson, Identification and quantification of the hydrological impacts of imperviousness in urban catchments: a review, J. Environ. Manag. 92 (6) (2011) 1438–1448, https://doi.org/10.1016/j.jenvman.2011.01.018.

[3] A.H. Elliott, S.A. Trowsdale, A review of models for low impact urban stormwater drainage, Environ. Model. Softw. 22 (3) (2007) 394–405, https://doi.org/10.1016/j.envsoft.2005.12.005.

[4] Y.-Y. Yang, G.S. Toor, Sources and mechanisms of nitrate and orthophosphate transport in urban stormwater runoff from residential catchments, Water Res. 112 (2017) 176–184, https://doi.org/10.1016/j.watres.2017.01.039.

[5] B. Brunekreef, S.T. Holgate, Air pollution and health, Lancet 360 (9341) (. 2002) 1233–1242, https://doi.org/10.1016/S0140-6736(02)11274-8.

[6] A. Kapoor, T. Viraraghavan, Nitrate removal from drinking water – review, J. Environ. Eng. 123 (4) (1997) 371–380, https://doi.org/10.1061/(ASCE)0733-9372(1997)123:4(371).

[7] W. H. Organization, Nitrate and nitrite in drinking-water: background document for development of WHO guidelines for drinking-water quality. Art. no. WHO/SDE/WSH/04.03/56, 2003, Accessed: Nov. 16, 2020. [Online]. Available: https://apps.who.int/iris/handle/10665/75380.

[8] O. US EPA, National Primary Drinking Water Regulation Table. US EPA, Jun. 07, 2016. https://www.epa.gov/ground-water-and-drinking-water/national-primary-drinking-water-regulation-table (accessed Nov. 16, 2020).

[9] L. Katata-Seru, T. Moremedi, O.S. Aremu, I. Bahadur, Green synthesis of iron nanoparticles using Moringa oleifera extracts and their applications: Removal of nitrate from water and antibacterial activity against Escherichia coli, J. Mol. Liq. 256 (2018) 296–304, https://doi.org/10.1016/j.molliq.2017.11.093.

[10] D.P. Durkin, et al., Sustainable and scalable natural fiber welded palladium-indium catalysts for nitrate reduction, Appl. Catal. B: Environ. 221 (2018) 290–301, https://doi.org/10.1016/j.apcatb.2017.09.029.

[11] Z. Shen, et al., Electrocatalytic reduction of nitrate in water using Cu/Pd modified Ni foam cathode: high nitrate removal efficiency and N2-selectivity, Sep. Purif. Technol. 241 (2020), 116743, https://doi.org/10.1016/j.seppur.2020.116743.

[12] K.M. Hiscock, J.W. Lloyd, D.N. Lerner, Review of natural and artificial denitrification of groundwater, Water Res. 25 (9) (1991) 1099–1111, https://doi.org/10.1016/0043-1354(91)90203-3.

[13] V. Matějů, S. Čižinská, J. Krejčí, T. Janoch, Biological water denitrification – a review, Enzym. Microb. Technol. 14 (3) (1992) 170–183, https://doi.org/10.1016/0141-0229(92)90062-S.

[14] Ş. Aslan, Combined removal of pesticides and nitrates in drinking waters using biodenitrification and sand filter system, Process Biochem. 40 (1) (2005) 417–424, https://doi.org/10.1016/j.procbio.2004.01.030.

[15] M. Shrimali, K.P. Singh, New methods of nitrate removal from water, Environ. Pollut. 112 (3) (2001) 351–359, https://doi.org/10.1016/S0269-7491(00)00147-0.

[16] N. Mahata, V. Vishwanathan, Influence of palladium precursors on structural properties and phenol hydrogenation characteristics of supported palladium catalysts, J. Catal. 196 (2) (2000) 262–270, https://doi.org/10.1006/jcat.2000.3041.

[17] H.A. Al-Wadhaf, V.M. Karpov, E.A. Katsman, Activity and selectivity of carbon supported palladium catalysts prepared from bis(η3-allyl)palladium complexes in phenylacetylene hydrogenation, Catal. Commun. 116 (2018) 67–71, https://doi.org/10.1016/j.catcom.2018.08.010.

[18] Q. Zhang, Y. Chu, X. Deng, L. Zhang, H. Chu, Improvement of a mesh-type Cu/Ni/γ-Al2O3/Al catalyst for steam reforming of dimethyl ether by metal (Fe, Zn or La) addition for CO in situ removal, Mod. Res. Catal. 7 (2018) 1, https://doi.org/10.4236/mrc.2018.71001.

[19] Z. Li, L. Shen, W. Huang, K. Xie, Kinetics of selective catalytic reduction of NO by NH3 on Fe-Mo/ZSM-5 catalyst, J. Environ. Sci. 19 (12) (2007) 1516–1519, https://doi.org/10.1016/S1001-0742(07)60247-2.

[20] M. Konsolakis, I.V. Yentekakis, NO reduction by propene or CO over alkali-promoted Pd/YSZ catalysts, J. Hazard. Mater. 149 (3) (2007) 619–624, https://doi.org/10.1016/j.jhazmat.2007.06.085.

[21] J.-I. Yang, H. Jung, The effect of temperature on NOx reduction by H2 in the presence of excess oxygen on a Pt/Al2O3 monolithic catalyst, Chem. Eng. J. 146 (1) (2009) 11–15, https://doi.org/10.1016/j.cej.2008.05.005.

[22] J.D.A. Bellido, E.M. Assaf, Reduction of NO by CO on Cu/ZrO2/Al2O3 catalysts: characterization and catalytic activities, Fuel 88 (9) (2009) 1673–1679, https://doi.org/10.1016/j.fuel.2009.04.015.

[23] S. Sitshebo, A. Tsolakis, K. Theinnoi, J. Rodríguez-Fernández, P. Leung, Improving the low temperature NOx reduction activity over a Ag-Al2O3 catalyst, Chem. Eng. J. 158 (3) (2010) 402–410, https://doi.org/10.1016/j.cej.2010.01.004.

[24] S. Pérez-Rodríguez, N. Rillo, M.J. Lázaro, E. Pastor, Pd catalysts supported onto nanostructured carbon materials for CO2 valorization by electrochemical reduction, Appl. Catal. B: Environ. 163 (2015) 83–95, https://doi.org/10.1016/j.apcatb.2014.07.031.

[25] N. Job, B. Heinrichs, F. Ferauche, F. Noville, J. Marien, J.-P. Pirard, Hydrodechlorination of 1,2-dichloroethane on Pd–Ag catalysts supported on tailored texture carbon xerogels, Catal. Today 102–103 (2005) 234–241, https://doi.org/10.1016/j.cattod.2005.02.021.

[26] S. Garcia-Segura, M. Lanzarini-Lopes, K. Hristovski, P. Westerhoff, Electrocatalytic reduction of nitrate: fundamentals to full-scale water treatment applications, Appl. Catal. B: Environ. 236 (2018) 546–568, https://doi.org/10.1016/j.apcatb.2018.05.041.

[27] S. Pérez-Rodríguez, M. Corengia, G. García, C.F. Zinola, M.J. Lázaro, E. Pastor, Gas diffusion electrodes for methanol electrooxidation studied by a new DEMS configuration: influence of the diffusion layer, Int. J. Hydrog. Energy 37 (8) (2012) 7141–7151, https://doi.org/10.1016/j.ijhydene.2011.11.090.

[28] D. Sebastián, et al., Influence of carbon nanofiber properties as electrocatalyst support on the electrochemical performance for PEM fuel cells, Int. J. Hydrog. Energy 35 (18) (2010) 9934–9942, https://doi.org/10.1016/j.ijhydene.2009.12.004.

[29] L. Calvillo, V. Celorrio, R. Moliner, M.J. Lázaro, Influence of the support on the physicochemical properties of Pt electrocatalysts: comparison of catalysts supported on different carbon materials, Mater. Chem. Phys. 127 (1) (2011) 335–341, https://doi.org/10.1016/j.matchemphys.2011.02.014.

[30] J.R.C. Salgado, F. Alcaide, G. Álvarez, L. Calvillo, M.J. Lázaro, E. Pastor, Pt–Ru electrocatalysts supported on ordered mesoporous carbon for direct methanol fuel cell, J. Power Sources 195 (13) (2010) 4022–4029, https://doi.org/10.1016/j.jpowsour.2010.01.001.

[31] M. Jesús Lázaro, et al., Carbon-based catalysts: synthesis and applications, Comptes Rendus Chim. 18 (11) (2015) 1229–1241, https://doi.org/10.1016/j.crci.2015.06.006.

[32] J. Soto-Hernández, et al., Electrochemical reduction of NOx species at the interface of nanostructured Pd and PdCu catalysts in alkaline conditions, Appl. Catal. B: Environ. 259 (2019) 118048, https://doi.org/10.1016/j.apcatb.2019.118048.

[33] P.B. Kettler, Platinum group metals in catalysis: fabrication of catalysts and catalyst precursors, Org. Process Res. Dev. 7 (3) (2003) 342–354, https://doi.org/10.1021/op034017o.

[34] B. Lesiak, et al., C sp2/sp3 hybridisations in carbon nanomaterials – XPS and (X) AES study, Appl. Surf. Sci. 452 (2018) 223–231, https://doi.org/10.1016/j.apsusc.2018.04.269.

[35] E. Antolini, Carbon supports for low-temperature fuel cell catalysts, Appl. Catal. B 88 (1-2) (2009) 1–24, https://doi.org/10.1016/j.apcatb.2008.09.030.

[36] S. Diodati, E. Negro, K. Vezzù, V. Di Noto, S. Gross, Oxygen reduction reaction and X-ray photoelectron spectroscopy characterisation of carbon nitride-supported bimetallic electrocatalysts, Electrochim. Acta 215 (2016) 398–409, https://doi.org/10.1016/j.electacta.2016.08.060.

[37] Y. Ji, Y. Ying, X. Guo, Y. Wu, Y. Wen, H. Yang, Palladium litchi-like nanoclusters for remarkably elevating methanol electrocatalytic activity, J. Power Sources 402 (2018) 183–188, https://doi.org/10.1016/j.jpowsour.2018.09.045.

[38] S. Kabir, A. Zadick, P. Atanassov, L. Dubau, M. Chatenet, Stability of carbon-supported palladium nanoparticles in alkaline media: A case study of graphitized and more amorphous supports, Electrochem. Commun. 78 (2017) 33–37, https://doi.org/10.1016/j.elecom.2017.03.017.

[39] A. Brouzgou, L.L. Yan, S.Q. Song, P. Tsiakaras, Glucose electrooxidation over PdxRh/C electrocatalysts in alkaline medium, Appl. Catal. B: Environ. 147 (2014) 481–489, https://doi.org/10.1016/j.apcatb.2013.09.024.

[40] J.L. Santos, C. Megías-Sayago, S. Ivanova, M.Á. Centeno, J.A. Odriozola, Functionalized biochars as supports for Pd/C catalysts for efficient hydrogen production from formic acid, Appl. Catal. B: Environ. 282 (2021), 119615, https://doi.org/10.1016/j.apcatb.2020.119615.

[41] H. Zhao, H. Li, H. Zhang, D. Zhao, Z. Zhu, Y. Zhao, Turning poison into medicine: NH3 or urea treatment leads to improved Pd-based three-way catalysts, Chem. Eng. J. 405 (2021), 126995, https://doi.org/10.1016/j.cej.2020.126995.

[42] C. Zhang, et al., Suppressing the Pd-C interaction through B-doping for highly efficient oxygen reduction, Carbon 149 (2019) 370–379, https://doi.org/10.1016/j.carbon.2019.04.060.

[43] J. Moreira, P. del Angel, A.L. Ocampo, P.J. Sebastián, J.A. Montoya, R.H. Castellanos, Synthesis, characterization and application of a Pd/Vulcan and Pd/C catalyst in a PEM fuel cell, Int. J. Hydrog. Energy 29 (9) (2004) 915–920, https://doi.org/10.1016/j.ijhydene.2003.06.003.

[44] M. Alesker, et al., Palladium/nickel bifunctional electrocatalyst for hydrogen oxidation reaction in alkaline membrane fuel cell, J. Power Sources 304 (2016) 332–339, https://doi.org/10.1016/j.jpowsour.2015.11.026.

[45] L. Pedraza-Segura, H. Toribio-Cuaya, A. Flores-Tlacuahuac, Multiobjective optimization approach for cellulosic biomass pretreatment, Ind. Eng. Chem. Res. 52 (15) (2013) 5357–5364, https://doi.org/10.1021/ie3032058.

[46] L. Pedraza, H. Toribio, R. Romo, S. Arreola, and M. Guevara, "Prebiotic Activity of Xylooligosaccharides from Corncob," p. 5.

[47] J.M. Dorhout, et al., NOx speciation from copper dissolution in nitric acid/water solutions using FTIR spectroscopy, J. Mol. Spectrosc. 372 (2020), 111334, https://doi.org/10.1016/j.jms.2020.111334.

[48] R.A. Stairs, Copper dissolution in nitric acid, J. Chem. Educ. 67 (2) (1990) 184, https://doi.org/10.1021/ed067p184.3.

[49] P.-C. Su, et al., Enhancement of electrochemical properties of Pd/C catalysts toward ethanol oxidation reaction in alkaline solution through Ni and Au alloying, Int. J. Hydrog. Energy 38 (11) (2013) 4474–4482, https://doi.org/10.1016/j.ijhydene.2013.01.173.

[50] D.J. Lim, N.A. Marks, M.R. Rowles, Universal Scherrer equation for graphene fragments, Carbon 162 (2020) 475–480, https://doi.org/10.1016/j.carbon.2020.02.064.

[51] W.-L. Qu, D.-M. Gu, Z.-B. Wang, J.-J. Zhang, High stability and high activity Pd/ITO-CNTs electrocatalyst for direct formic acid fuel cell, Electrochim. Acta 137 (2014) 676–684, https://doi.org/10.1016/j.electacta.2014.06.064.

[52] J.C. Bertolini, P. Delichere, B.C. Khanra, J. Massardier, C. Noupa, B. Tardy, Electronic properties of supported Pd aggregates in relation with their reactivity for 1,3-butadiene hydrogenation, Catal. Lett. 6 (2) (1990) 215–223, https://doi.org/10.1007/BF00774723.

[53] L.S. Kibis, A.I. Titkov, A.I. Stadnichenko, S.V. Koscheev, A.I. Boronin, X-ray photoelectron spectroscopy study of Pd oxidation by RF discharge in oxygen, Appl. Surf. Sci. 255 (22) (2009) 9248–9254, https://doi.org/10.1016/j.apsusc.2009.07.011.

[54] L.P.A. Guerrero-Ortega, et al., Pd and Pd@PdO core–shell nanoparticles supported on Vulcan carbon XC-72R: comparison of electroactivity for methanol electro-oxidation reaction, J. Mater. Sci. vol. 54 (21) (2019) 13694–13714, https://doi.org/10.1007/s10853-019-03843-8.

[55] A. Theodosiou, B.F. Spencer, J. Counsell, A.N. Jones, "An XPS/UPS study of the surface/near-surface bonding in nuclear grade graphites: a comparison of monatomic and cluster depth-profiling techniques,", Appl. Surf. Sci. 508 (2020), 144764 https://doi.org/10.1016/j.apsusc.2019.144764.

[56] S.T. Jackson, R.G. Nuzzo, Determining hybridization differences for amorphous carbon from the XPS C 1s envelope, Appl. Surf. Sci. 90 (2) (1995) 195–203, https://doi.org/10.1016/0169-4332(95)00079-8.

[57] H. Luo, H. Fu, H. Yin, Q. Lin, Carbon materials in persulfate-based advanced oxidation processes: the roles and construction of active sites, J. Hazard. Mater. (2021), 128044, https://doi.org/10.1016/j.jhazmat.2021.128044.

[58] D.J. Morgan, Cluster cleaned HOPG by XPS, Surf. Sci. Spectra 24 (2) (2017), 024003, https://doi.org/10.1116/1.4993771.

[59] J.C. Lascovich, S. Scaglione, Comparison among XAES, PELS and XPS techniques for evaluation of Sp2 percentage in a-C:H, Appl. Surf. Sci. 78 (1) (1994) 17–23, https://doi.org/10.1016/0169-4332(94)90026-4.

[60] L. Fang, Q. Tao, M. Li, L. Liao, D. Chen, Y. Chen, Determination of the real surface area of palladium electrode, Chin. J. Chem. Phys. 23 (5) (2010) 543–548, https://doi.org/10.1088/1674-0068/23/05/543-548.

[61] A. Zadick, L. Dubau, U. Demirci, M. Chatenet, Effects of Pd nanoparticle size and solution reducer strength on Pd/C electrocatalyst stability in alkaline electrolyte,

J. Electrochem. Soc. 163 (8) (2016) F781–F787, https://doi.org/10.1149/2.0141608jes.

[62] D.A.J. Rand, R. Woods, The nature of adsorbed oxygen on rhodium, palladium and gold electrodes, J. Electroanal. Chem. Interfacial Electrochem. 31 (1) (1971) 29–38, https://doi.org/10.1016/S0022-0728(71)80039-6.

[63] A.N. Correia, L.H. Mascaro, S.A.S. Machado, L.A. Avaca, Active surface area determination of Pd-Si alloys by H-adsorption, Electrochim. Acta 42 (3) (1997) 493–495, https://doi.org/10.1016/S0013-4686(96)00232-0.

[64] J. Sá, J.A. Anderson, FTIR study of aqueous nitrate reduction over Pd/TiO2, Appl. Catal. B: Environ. 77 (3) (2008) 409–417, https://doi.org/10.1016/j.apcatb.2007.08.013.

[65] G.E. Dima, G.L. Beltramo, M.T.M. Koper, Nitrate reduction on single-crystal platinum electrodes, Electrochim. Acta 50 (21) (2005) 4318–4326, https://doi.org/10.1016/j.electacta.2005.02.093.

[66] S. Goldstein, D. Behar, T. Rajh, J. Rabani, Nitrite reduction to nitrous oxide and ammonia by TiO2 electrons in a colloid solution via consecutive one-electron transfer reactions, J. Phys. Chem. A 120 (15) (2016) 2307–2312, https://doi.org/10.1021/acs.jpca.6b01761.

[67] H. Lan, X. Liu, H. Liu, R. Liu, C. Hu, J. Qu, Efficient nitrate reduction in a fluidized electrochemical reactor promoted by Pd–Sn/AC particles, Catal. Lett. 146 (1) (2016) 91–99, https://doi.org/10.1007/s10562-015-1615-3.

[68] A.S. Dutton, J.M. Fukuto, K.N. Houk, Theoretical reduction potentials for nitrogen oxides from CBS-QB3 energetics and (C)PCM solvation calculations, Inorg. Chem. 44 (11) (2005) 4024–4028, https://doi.org/10.1021/ic048734q.

[69] P.M. Tucker, M.J. Waite, B.E. Hayden, Electrocatalytic reduction of nitrate on activated rhodium electrode surfaces, J. Appl. Electrochem. 34 (8) (2004) 781–796, https://doi.org/10.1023/B:JACH.0000035607.19248.b6.

[70] A.C.A. de Vooys, G.L. Beltramo, B. van Riet, J.A.R. van Veen, M.T.M. Koper, Mechanisms of electrochemical reduction and oxidation of nitric oxide, Electrochim. Acta 49 (8) (2004) 1307–1314, https://doi.org/10.1016/j.electacta.2003.07.020.